will be further reduced using the present technique.

Holt and Krotkov,[11] while reporting their measurements on excitation cross sections in helium, also calculated $K = 0.89 \pm 0.04$. We obtained $K = 0.89 \pm 0.03$ by neglecting the electric field perturbation of the ground state; inclusion of this correction resulted in $K = 0.92 \pm 0.03$ as reported in Sec. II. Their observed transmission curve for $2\,^1S_0$ atoms corresponds to a value of K well below ours; this is due to poorly known velocity distribution and plate separation, neither of which was important to their main work.

It was suggested to us that metastable He quenching could serve as a useful method for measuring electric fields in a beam apparatus, since often other considerations of the experiment make it difficult to know the effective plate separation accurately.[12] Having measured the transmission of Eq. (6) with $K = 0.926 \pm .020$ gives the field strength uniquely if the velocity distribution is known.

*Work supported by the National Science Foundation.

[1]R. S. Van Dyck, Jr., C. E. Johnson, and H. A. Shugart, Phys. Rev. Letters 25, 1403 (1970).

[2]W. E. Lamb, Jr. and R. C. Retherford, Phys. Rev. 72, 241 (1947).

[3]A. Dalgarno and N. Lynn, Proc. Phys. Soc. (London) A70, 802 (1957).

[4]K. T. Chung and R. P. Hurst, Phys. Rev. 152, 35 (1966).

[5]A. Dalgarno and A. E. Kingston, Proc. Phys. Soc. (London) A72, 1053 (1958).

[6]S. Huang, Astrophys. J. 108, 354 (1948).

[7]We would like to thank B. Schiff for sending us a report of his and Pekeris's work [Schiff and Pekeris (unpublished)]. Using their newly calculated oscillator strength between the m^1S_0 and n^1P_1 states in Eq. (3), for $m = 1$ and 2 and $n = 4$ and 5, instead of the corresponding f values of Table I, we arrived at essentially the same values for K.

[8]J. Burger and A. Lurio recently measured the oscillator strength between the 1^1S_0 and n^1P_1 state, for $n = 2$ and 3. Their results are in excellent agreement with the calculated values of Schiff and Pekeris which are given in Table I. The details of Burger and Lurio's experiment are to be found in Phys. Rev. A 3, 64 (1971).

[9]We would like to thank Harvey Gould of Brandeis University who designed and built the electric field plates.

[10]R. T. Robiscoe and T. W. Shyn, Phys. Rev. Letters 24, 559 (1970).

[11]H. K. Holt and R. Krotkov, Phys. Rev. 144, 82 (1966).

[12]A. Lurio (private communication).

PHYSICAL REVIEW A VOLUME 5, NUMBER 1 JANUARY 1972

Magnetic Moment of the Proton in Bohr Magnetons*

P. Frank Winkler,† Daniel Kleppner,‡ Than Myint,§ and Frederick G. Walther‡

Research Laboratory of Electronics, Massachusetts Institute of Technology, Cambridge, Massachusetts 02139

(Received 8 September 1971)

The magnetic moment of the proton has been measured by observing simultaneously an electronic and a nuclear magnetic transition in atomic hydrogen. Observations were made with a hydrogen maser operating in a 3500-G field. A theory is presented for the transient response of a three-level system under conditions of double resonance including effects of cavity pulling, spin-exchange collisions, and frequency shifts due to motional field narrowing. The electron-proton g-factor ratio in hydrogen is found to be $g_j(\mathrm{H})/g_p(\mathrm{H}) = \mu_j(\mathrm{H})/\mu_p(\mathrm{H}) = -658.210\,706\ (6)$. This leads to a value of the proton moment in Bohr magnetons of $\mu_p/\mu_B = 1.521\,032\,181\ (15) \times 10^{-3}$.

I. INTRODUCTION

Precise measurement of the ratio of the magnetic moments of the electron and proton, μ_e/μ_p, is important for both atomic and molecular physics. Knowledge of μ_e/μ_p is needed in the calculation of the hyperfine structure of hydrogen which, because of its simplicity, is widely used in testing physical theories. The ratio is also used as a transfer standard when a magnetic field must be determined in atomic units. Since μ_e is known to high precision in terms of the Bohr magneton, measurement of μ_e/μ_p gives an absolute value for the proton moment. Furthermore, by comparing the values of μ_e/μ_p as observed in various molecular environments with the value in atomic hydrogen, the molecular diamagnetic shielding of the proton can be determined absolutely to high precision, thus allowing a detailed check on the theory of chemical shifts. In a similar fashion, effects of binding on the magnetic moment of the electron can be observed by comparing μ_e/μ_p for the electron bound in hydrogen and for the free electron. Finally, the value of the electron-to-proton magnetic-moment

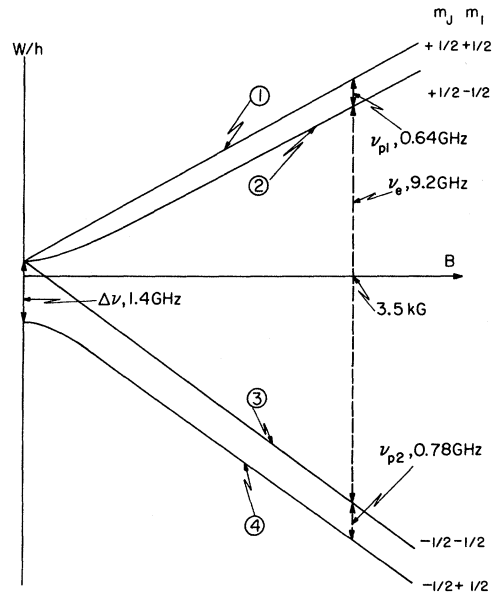

FIG. 1. Energy levels of hydrogen in the ground electronic state in an applied magnetic field.

ratio is useful as an auxiliary constant in the evaluation of the table of fundamental constants.

We present the results of a determination of $\mu_e(\mathrm{H})/\mu_p(\mathrm{H})$, the ratio of the electron moment to the proton moment as observed in the ground state of atomic hydrogen. The measurement was made by observing simultaneously electron and proton transitions with a hydrogen maser operating in an applied magnetic field of 3500 G. It differs from previous measurements in over-all precision and in the fact that the proton was observed in atomic hydrogen rather than in a molecular environment. In previous measurements the proton transitions were observed by NMR in water or some equivalent medium, and the results are subject to a large uncertainty because of the need for molecular shielding corrections. Furthermore, these measurements involved interchange of samples in a fixed magnetic field, a procedure susceptible to systematic error. (Reference to earlier work will be given in a later section.)

The proton moment has not been previously measured in atomic hydrogen because the hyperfine interaction dominates over the coupling of the proton to the external field and results in what was a prohibitive loss of sensitivity; the proton transition frequencies require a fractional accuracy about 50 times greater than the final accuracy in μ_e/μ_p. However, the narrow electron transition linewidths achievable with the hydrogen maser, 100 Hz, compared to a typical value of 30 kHz for previous methods, enable precise measurement in spite of the adverse effect of hyperfine coupling.

The hydrogen maser is operated on an "electron transition" denoted ν_e in Fig. 1. At the same time, one of the "proton transitions" ν_{p1} or ν_{p2} is observed by double resonance. As we shall show, knowledge of ν_e along with either ν_{p1} or ν_{p2} is sufficient to determine μ_e/μ_p. Owing to the short relaxation times resulting from its small physical dimensions and the effects of magnetic field inhomogeneities, our maser does not oscillate. Instead we use a pulse technique and observe the free-precession decay signal at the electron transition frequency. Continuous stimulation of a proton transition by an applied rf signal results in amplitude modulation of the free-precession signal.

Results of an early version of this experiment have previously been reported[1] as have preliminary results of the present work.[2,3] Further description of the experiment and apparatus are presented in theses by two of the authors.[4,5] In the following sections we describe the theory of the measurement procedure, give experimental details, and present the final results and their interpretation.

II. THEORY OF EXPERIMENT

A. Preliminaries

The magnetic moment of the electron in a state with angular momentum $\hbar\vec{J}$ is $\vec{\mu}_j = g_j\mu_B\vec{J}$, where μ_B is the Bohr magneton and g_j is the electronic g factor. Similarly, we can write the proton moment as $\vec{\mu}_p = g_p\mu_B\vec{I}$. The quantity of interest is the negative ratio of the magnetic moments, R:

$$R \equiv -\frac{\mu_j}{\mu_p} = -\frac{g_j}{g_p}\frac{J}{I} . \tag{1}$$

R is intrinsically positive since the electron moment is negative and the proton moment is positive. In the ground state of hydrogen $J = I = \frac{1}{2}$, and $R = -g_j(\mathrm{H})/g_p(\mathrm{H})$.

The Hamiltonian for the magnetic interaction of hydrogen in the ground state in the presence of an external magnetic field $\vec{H}_0$ is taken to be

$$\mathcal{H} = ha\vec{I}\cdot\vec{J} - g_j(\mathrm{H})\,\mu_B\vec{J}\cdot\vec{H}_0 - g_p(\mathrm{H})\mu_B\vec{I}\cdot\vec{H}_0 , \tag{2}$$

where a is the hyperfine interaction constant. For the case $J = \frac{1}{2}$, $a = \nu_0$, the hyperfine frequency. The energy states of this Hamiltonian are given by the well-known Breit-Rabi equation.[6] The energy levels in frequency units are

$$\begin{aligned}
\nu_1 &= \tfrac{1}{4}\nu_0(1+2x) - \nu_p , \\
\nu_2 &= -\tfrac{1}{4}\nu_0 + \tfrac{1}{2}\nu_0(1+x^2)^{1/2} , \\
\nu_3 &= \tfrac{1}{4}\nu_0(1-2x) + \nu_p , \\
\nu_4 &= -\tfrac{1}{4}\nu_0 - \tfrac{1}{2}\nu_0(1+x^2)^{1/2} ,
\end{aligned} \tag{3}$$

where $\nu_p = g_p(\mathrm{H})\,\mu_0 H_0/h$ is the NMR frequency for

protons in the field H_0, and x is a dimensionless magnetic field parameter:

$$x=\left(\frac{-\mu_J}{J}+\frac{\mu_p}{I}\right)\frac{H_0}{h\nu_0}=(R+1)\frac{\nu_p}{\nu_0}\,. \tag{4}$$

The energy levels are identified in Fig. 1.

Equations (3) involve the three parameters ν_0, x, and ν_p, and in principle three transition frequencies must be measured to determine all the unknowns. Fortunately, the hyperfine frequency ν_0 is independently known to high precision, so that only two measurements are required. However, in order to minimize certain systematic errors, we actually measured the three transitions indicated in Fig. 1. The transition frequencies are given by

$$\begin{aligned}\nu_{p1}&=\tfrac{1}{2}\nu_0\left[1+x-(1+x^2)^{1/2}\right]-\nu_p\,,\\ \nu_{p2}&=\tfrac{1}{2}\nu_0\left[1-x+(1+x^2)^{1/2}\right]+\nu_p\,,\\ \nu_e&=\tfrac{1}{2}\nu_0\left[x-1+(1+x^2)^{1/2}\right]-\nu_p\,.\end{aligned} \tag{5}$$

The "proton transitions" ν_{p1} and ν_{p2} are dominated by the hyperfine coupling terms. In contrast, the "electron transition" ν_e is due chiefly to interaction of the electron with the applied field. The relative size of these interactions becomes apparent if we expand Eqs. (5) in the limit of high field, $x\gg 1$:

$$\begin{aligned}\nu_{p1}&=\tfrac{1}{2}\nu_0\left(1-1/2x-\cdots\right)-\nu_p\,,\\ \nu_{p2}&=\tfrac{1}{2}\nu_0\left(1+1/2x+\cdots\right)+\nu_p\,,\\ \nu_e&=\tfrac{1}{2}\nu_0\left(2x-1+\cdots\right)-\nu_p\,.\end{aligned} \tag{6}$$

$\nu_0=1.4$ GHz. In our experiment $H_0=3500$ G, $x=7$, $\nu_p=15$ MHz, ν_{p1}, $\nu_{p2}\approx 700$ MHz, and $\nu_e=9.2$ GHz. The interaction of the proton with the applied field ν_p is approximately 2% of its hyperfine interaction.

The g-factor ratio R is determined from the measured transition frequencies by

$$R=-\frac{g_j(\mathrm{H})}{g_p(\mathrm{H})}=\frac{y+1}{y-1}\,, \tag{7}$$

where y depends on the proton transition as follows:

$$\begin{aligned}y_{p1}&=\frac{\nu_e-\nu_{p1}}{\nu_e+\nu_{p1}}\left(1+\frac{2\nu_0}{\nu_e-\nu_{p1}}\right)^{1/2}\,,\\ y_{p2}&=\frac{\nu_e-\nu_0+\nu_{p2}}{\nu_e+\nu_0-\nu_{p2}}\left(1+\frac{2\nu_0}{\nu_e-\nu_0+\nu_{p2}}\right)^{1/2}\,.\end{aligned} \tag{8}$$

Since $\nu_{p1}+\nu_{p2}=\nu_0$, these equations are redundant. However, as shown in Sec. II F, this is no longer true when certain sources of experimental error are considered.

Because $\nu_p\ll\nu_0$, the proton transition must be determined to a relative precision 25 times higher than the electron transition, or an absolute precision 300 times higher. Consequently, the major experimental effort lay in determining ν_{p1} and ν_{p2}.

B. Governing Equations for Maser

1. *Evolution of the Density Matrix*

The radiating system contains an ensemble of atoms in some combination of the four states described by Eqs. (3). In addition to the static field H_0, an oscillating magnetic field induces the electron transition (2-3) and a second oscillating field induces a proton transition, either (1-2) or (3-4). The system is also affected by the flow of atoms to the storage bulb and by relaxation effects such as those due to spatial inhomogeneities in the static field. Our task is to analyze the response of this system to the applied fields.

The system is most conveniently described with a density-matrix formalism following a procedure previously used in the analysis of hydrogen-maser problems.[7,8] The evolution in time of the density matrix can be decomposed as follows:

$$\dot\rho=\dot\rho_{\text{radiation}}+\dot\rho_{\text{relaxation}}+\dot\rho_{\text{flow}}+\dot\rho_{\text{spin exchange}}\,. \tag{9}$$

We shall consider each contribution in turn, deferring the relatively minor spin-exchange contribution until Sec. II G. In the absence of spin exchange only three of the four states play a role at a given time; consequently we need deal with only a 3×3 matrix. If ν_{p1} and ν_e are under observation, the states involved are (1, 2, 3); if ν_{p2} and ν_e are being observed, the states are (2, 3, 4). We consider the former case first.

The transition (1-2) at frequency ν_{p1} is induced by an oscillating magnetic field $\vec{H}_1\cos\Omega t$, while the transition (2-3) at frequency ν_e is induced by a field $\vec{H}_2\cos\omega t$. $\vec{H}_1$ and $\vec{H}_2$ are perpendicular to the static field $\vec{H}_0$. The matrix elements of the Hamiltonian describing the radiation interactions are

$$\begin{aligned}\langle 1|\mathcal{H}_{\text{rad}}|2\rangle&=-\tfrac{1}{4}g_p\mu_B H_1 e^{-i\Omega t}\,,\\ \langle 2|\mathcal{H}_{\text{rad}}|3\rangle&=-\tfrac{1}{4}g_j\mu_B H_2 e^{-i\omega t}\,.\end{aligned} \tag{10}$$

For the present we are neglecting effects of the counter-rotating field and of fields far from resonance. The matrix elements are correct in the limit $H_0\to\infty$, and are sufficiently accurate for our purposes. We can rewrite the matrix elements in reduced form

$$\begin{aligned}\langle 1|\mathcal{H}_{\text{rad}}|2\rangle&=\tfrac{1}{2}\hbar X e^{-i\Omega t}\,,\\ \langle 2|\mathcal{H}_{\text{rad}}|3\rangle&=\tfrac{1}{2}\hbar x e^{-i\omega t}\,,\end{aligned} \tag{11}$$

where

$$\begin{aligned}X&=-g_p\mu_B H_1/2\hbar\,,\\ x&=-g_j\mu_B H_2/2\hbar\,.\end{aligned} \tag{12}$$

[The same symbol x is used for the field parameter defined in Eq. (4) and the reduced matrix element for the electron transition (12). The meaning should be clear from the context.] $\dot{\rho}_{\text{radiation}}$ is then given by

$$\begin{aligned}
\dot{\rho}_{11} &= -\operatorname{Im}(X^*\rho_{12}e^{i\Omega t}) ,\\
\dot{\rho}_{22} &= \operatorname{Im}(X^*\rho_{12}e^{i\Omega t}) - \operatorname{Im}(x^*\rho_{23}e^{i\omega t}) ,\\
\dot{\rho}_{33} &= \operatorname{Im}(x^*\rho_{23}e^{i\omega t}) ,\\
\dot{\rho}_{12} &= -i\Omega_0\rho_{12} + \tfrac{1}{2}iX(\rho_{11}-\rho_{22})e^{-i\Omega t} + \tfrac{1}{2}ix^*\rho_{13}e^{i\omega t},\\
\dot{\rho}_{23} &= -i\omega_0\rho_{23} + \tfrac{1}{2}ix(\rho_{22}-\rho_{33})e^{-i\omega t} - \tfrac{1}{2}iX^*\rho_{13}e^{i\Omega t},\\
\dot{\rho}_{13} &= -i(\Omega_0+\omega_0)\rho_{13} - \tfrac{1}{2}iX\rho_{23}e^{-i\Omega t} + \tfrac{1}{2}ix\rho_{12}e^{-i\omega t} ,
\end{aligned} \tag{13}$$

where $\Omega_0 = 2\pi\nu_{p1}$, $\omega_0 = 2\pi\nu_e$.

The dominant relaxation process for the electrons is dephasing of the oscillating moments as the atoms move randomly through the residual gradients in the static field. Under certain conditions this leads to a transverse relaxation rate given by[9]

$$1/\tau_2(i,j) = \gamma_{ij}^2\langle\Delta H_0^2\rangle\tau_c . \tag{14}$$

$\gamma_{ij} = \partial\omega_{ij}/\partial H_0$ is the gyromagnetic ratio for the transition $(i\text{-}j)$, $\langle\Delta H_0^2\rangle$ is the mean-square field inhomogeneity, and τ_c is a correlation time approximately equal to the mean collision time. (At the low densities involved atom-atom collisions are negligible and τ_c represents the mean time for collisions with the walls.) It should be emphasized that this result is not rigorous and that departures from it are significant in our experiment. However, it is adequate for the present.

Transitions (1-3) and (2-3) have a similar magnetic field dependence, and we designate their transverse relaxation rate by τ_2^{-1}. Because of the small field dependence of transition (1-2), its transverse relaxation can be neglected. The collision rate is so small compared to the transition frequencies that longitudinal relaxation due to motion through magnetic field inhomogeneities is negligible. The relaxation term is thus given simply by

$$\dot{\rho}_{\text{relaxation}} = -\frac{1}{\tau_2}\begin{bmatrix} 0 & 0 & \rho_{13} \\ 0 & 0 & \rho_{23} \\ \rho_{31} & \rho_{32} & 0 \end{bmatrix} . \tag{15}$$

The atomic beam provides a source of atoms equally distributed between the states (1) and (2). If we designate the mean time an atom spends in the bulb by τ_g (the "geometric lifetime"), then

$$\dot{\rho}_{\text{flow}} = \begin{bmatrix} \frac{1}{\tau_g} & \frac{1}{2} & \\ & \frac{1}{2} & \\ & & 0 \end{bmatrix} - \frac{1}{\tau_g}\rho . \tag{16}$$

In combining Eqs. (9), (13), (15), and (16) some simplification can be achieved by writing the diagonal elements as population differences:

$$\mathcal{P}_1 = \rho_{11} - \rho_{22} , \quad \mathcal{P}_2 = \rho_{22} - \rho_{33} . \tag{17}$$

The result is the following set of rate equations:

$$\begin{aligned}
\dot{\mathcal{P}}_1 &= -\gamma\mathcal{P}_1 - 2\operatorname{Im}(X^*\rho_{12}e^{i\Omega t}) + \operatorname{Im}(x^*\rho_{23}e^{i\omega t}) ,\\
\dot{\mathcal{P}}_2 &= -\gamma\mathcal{P}_2 + \operatorname{Im}(X\rho_{12}e^{i\Omega t}) - 2\operatorname{Im}(x^*\rho_{23}e^{i\omega t}) ,\\
\dot{\rho}_{12} &= -\gamma\rho_{12} - i\Omega_0\rho_{12} + \tfrac{1}{2}iX^*\mathcal{P}_1e^{-i\Omega t} + \tfrac{1}{2}ix^*\rho_{13}e^{i\omega t} ,\\
\dot{\rho}_{23} &= -\Gamma\rho_{23} - i\omega_0\rho_{23} + \tfrac{1}{2}ix\mathcal{P}_2e^{-i\omega t} - \tfrac{1}{2}iX\rho_{13}e^{i\Omega t} ,\\
\dot{\rho}_{13} &= -\Gamma\rho_{13} - i(\Omega_0+\omega_0)\rho_{13} - \tfrac{1}{2}iX\rho_{23}e^{-i\Omega t} + \tfrac{1}{2}ix\rho_{12}e^{-i\omega t} ,
\end{aligned} \tag{18}$$

where

$$\gamma = 1/\tau_g \text{ and } \Gamma = (1/\tau_g + 1/\tau_2) .$$

2. *Feedback Relations*

In the absence of an applied oscillating field the electron transition is sustained by the cavity field whose source is the radiating electron moments. The power P radiated at the electron transition frequency is the product of the number of radiators, photon energy, and radiation rate:

$$\begin{aligned}
P &= (I/\gamma)\hbar\omega(-\dot{\rho}_{22})_{\text{rad}}\\
&= (I/\gamma)\hbar\omega\operatorname{Im}(x^*\rho_{23}e^{i\omega t}) ,
\end{aligned} \tag{19}$$

where we have included only the contribution to $(\dot{\rho}_{22})_{\text{rad}}$ occurring at frequency ω. I is the total flux of atoms into the bulb.

If we let W represent the oscillatory magnetic energy stored in the cavity, then the energy balance is given by

$$\frac{dW}{dt} = P - \frac{\omega W}{Q} . \tag{20}$$

The last term represents the total power loss due to all dissipative mechanisms. The time variation of P is limited by the atomic-resonance linewidth, 2Γ, which is small compared to the width of the cavity mode ω/Q ($2\Gamma Q/\omega \sim 10^{-4}$). Consequently we can consider quasistationary solutions to Eq. (20) where we neglect dW/dt. This yields

$$P = (1/8\pi)\langle H_1^2\rangle_c V_c\omega/Q . \tag{21}$$

The average is over the cavity volume V_c. This expression assumes that the cavity is tuned close to the electron transition frequency so that $\omega \approx \omega_0$. Since the rotating magnetization is proportional to the driving field, we can write

$$\rho_{23}e^{i\omega t} = (ix/2K)e^{-i\varphi} . \tag{22}$$

K is a proportionality constant yet to be determined. The phase factor i is introduced to allow for the

quadrature relation between magnetization and field at resonance, while φ represents a phase shift due to cavity mistuning

$$\varphi = \arctan[(2Q/\omega)(\omega - \omega_c)] . \tag{23}$$

If we take $\varphi = 0$, Eqs. (12), (18), (21), and (22) yield

$$K = \frac{\pi I \mu_B^2 g_s^2 Q\eta}{\gamma V_c \hbar} , \tag{24}$$

where[10] $\eta = \langle H_x \rangle_b^2 / \langle H^2 \rangle_c$. $\langle H_x \rangle_b$ indicates the average of H_x over the storage bulb volume.

3. *Governing Equations*

We can remove the explicit time dependence from the rate equations by writing the off-diagonal elements in the following form:

$$\begin{aligned} \rho_{12} &= (D_1 + iD_2)\, e^{-i\Omega t} , \\ \rho_{23} &= (D_3 + iD_4)\, e^{-i\omega t} , \\ \rho_{13} &= (D_5 + iD_6)\, e^{-i(\Omega+\omega)t} . \end{aligned} \tag{25}$$

The matrix elements D_j are taken to be real. It is convenient to write the oscillating field amplitude in terms of real variables as

$$x/2K = \alpha + i\beta . \tag{26}$$

Equation (16) can then be rewritten as

$$\begin{aligned} \dot{\mathcal{O}}_1 &= -\gamma \mathcal{O}_1 - 2XD_2 + 2K(\alpha D_4 - \beta D_3) , \\ \dot{\mathcal{O}}_2 &= -\gamma \mathcal{O}_2 + XD_2 - 4K(\alpha D_4 - \beta D_3) + \tfrac{1}{2}\gamma , \\ \dot{D}_1 &= -\gamma D_1 - \Delta D_2 + K(\beta D_5 - \alpha D_6) , \\ \dot{D}_2 &= -\gamma D_2 + \Delta D_1 + \tfrac{1}{2}X\mathcal{O}_1 + K(\alpha D_5 + \beta D_6) , \\ \dot{D}_3 &= -\Gamma D_3 - \delta D_4 + \tfrac{1}{2}XD_6 - K\beta \mathcal{O}_2 , \\ \dot{D}_4 &= -\Gamma D_4 + \delta D_3 - \tfrac{1}{2}XD_5 + K\alpha \mathcal{O}_2 , \\ \dot{D}_5 &= -\Gamma D_5 - (\Delta + \delta) D_6 + \tfrac{1}{2}XD_4 - K(\beta D_1 + \alpha D_2) , \\ \dot{D}_6 &= -\Gamma D_6 + (\Delta + \delta) D_5 - \tfrac{1}{2}XD_3 + K(\alpha D_1 - \beta D_2) . \end{aligned} \tag{27}$$

Here $\Delta = \Omega - \Omega_0$ and $\delta = \omega - \omega_0$. This set of eight nonlinear coupled equations governs the dynamical behavior of the radiating system. The observed power is given by Eqs. (19), (23), (25), and (26),

$$P = (2KI/\gamma)\hbar\omega(D_3^2 + D_4^2)\cos\varphi . \tag{28}$$

4. *Threshold Conditions*

Although the maser has not been operated in a condition of stationary oscillation, the threshold atomic flux for oscillation I_{th} is a useful parameter for characterizing the operating level. This is readily found from the time-independent solution to Eqs. (27) which satisfies $P \geq 0$, assuming that no radiation field is applied at the proton transition (i.e., $X = 0$). The result is

$$K \geq 2\Gamma , \tag{29}$$

which gives

$$I_{th} = \frac{2\gamma\Gamma V_c \hbar}{\pi \mu_B^2 g_s^2 Q\eta} . \tag{30}$$

C. Transient Operation

1. *Preparation of System*

The system can be prepared in a radiating state by applying a short pulse near the electron transition frequency. In general this is chosen to be of length $\tau \ll \Gamma^{-1}$. The intensity of the applied microwave field, which we write as x_0, is sufficiently large that $x_0 \gg (X, \gamma, \Gamma)$. We take the pulse to act from $t = -\tau$ to $t = 0$. If the initial value of the density matrix is given by flow equilibrium

$$\rho(t < -\tau) = \begin{bmatrix} \frac{1}{2} & & \\ & \frac{1}{2} & \\ & & 0 \end{bmatrix} , \tag{31}$$

then the solutions to Eqs. (27) at $t = 0$ are

$$\begin{aligned} \mathcal{O}_1(0) &= \tfrac{1}{4}[1 - 2\mathcal{O}_2(0)] , \\ \mathcal{O}_2(0) &= (1/2a^2)(\delta^2 + x_0^2 \cos a\tau) , \\ D_3(0) &= -(x\delta/4a^2)(1 - \cos a\tau) , \\ D_4(0) &= (x/4a)\sin a\tau , \end{aligned} \tag{32}$$

where $a = (x_0^2 + \delta^2)^{1/2}$. In most cases the frequency of the applied pulse is close to resonance ($\delta \ll x_0$), so that Eqs. (32) can be rewritten to a good approximation as

$$\begin{aligned} &\mathcal{O}_1(0) = \tfrac{1}{4}(1 - \cos\theta), \quad \mathcal{O}_2(0) = \tfrac{1}{2}\cos\theta , \\ &D_4(0) = \tfrac{1}{4}\sin\theta , \qquad D_j(0) = 0, \quad j \neq 4 , \end{aligned} \tag{33}$$

where $\theta = a\tau \approx x_0\tau$. The pulse length τ is normally adjusted such that the subsequent radiated power is close to maximum ($\theta \approx \frac{1}{2}\pi$).

2. *Free Precession in Low-Flux Limit*

The governing equations (27) are nonlinear and cannot be solved in closed form. However, the characteristic transient behavior of the system can be understood by considering the low-flux limit where $K \ll \gamma, T$. Physically, neglecting K is equivalent to assuming that the contribution to the oscillating moment of atoms which enter after the pulse is negligible. In this case the governing equations can be decomposed into two groups of linear equations:

$$\begin{bmatrix} \dot{\mathcal{P}}_1 \\ \dot{\mathcal{P}}_2 \\ \dot{D}_1 \\ \dot{D}_2 \end{bmatrix} = \begin{bmatrix} -\gamma & & & -2X \\ & -\gamma & & X \\ & & -\gamma & -\Delta \\ \tfrac{1}{2}X & & \Delta & -\gamma \end{bmatrix} \begin{bmatrix} \mathcal{P}_1 \\ \mathcal{P}_2 \\ D_1 \\ D_2 \end{bmatrix} + \begin{bmatrix} 0 \\ \tfrac{1}{2}\gamma \\ 0 \\ 0 \end{bmatrix}, \tag{34}$$

$$\begin{bmatrix} \dot{D}_3 \\ \dot{D}_4 \\ \dot{D}_5 \\ \dot{D}_6 \end{bmatrix} = \begin{bmatrix} -\Gamma & -\delta & & \tfrac{1}{2}X \\ \delta & -\Gamma & -\tfrac{1}{2}X & \\ & \tfrac{1}{2}X & -\Gamma & -(\Delta+\delta) \\ -\tfrac{1}{2}X & & (\Delta+\delta) & -\Gamma \end{bmatrix} \begin{bmatrix} D_3 \\ D_4 \\ D_5 \\ D_6 \end{bmatrix}. \tag{35}$$

We now investigate the rotating electron magnetization under double-resonance conditions, i.e., while the proton transition is stimulated by an rf field X. We expect that the magnetization will depend on X and on Δ, the rf frequency deviation. Furthermore, we expect that the solution will reduce to an exponential decay in the limits $X=0$ or $\Delta \to \pm\infty$.

The solutions for D_3 and D_4 obtained from Eq. (35) are

$$D_3 = (\sin\theta/8A)\, e^{-\Gamma t}\,[(A+\Delta)\sin\tfrac{1}{2}(A-\Delta-2\delta)t - (A-\Delta)\sin\tfrac{1}{2}(A+\Delta+2\delta)t\,],$$

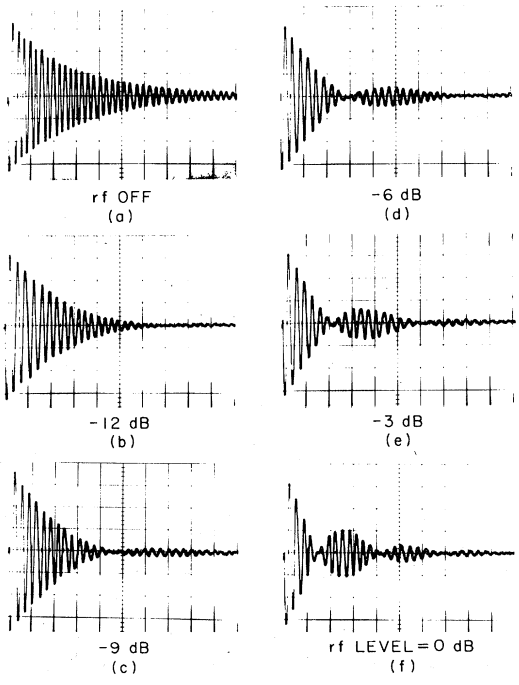

FIG. 2. Oscilloscope traces of electron free-precession signal during double resonance. The proton transition is stimulated by a signal at resonance with the relative power levels indicated. The high-frequency carrier is introduced for ease of display and detection. Time scale: 2 msec/division.

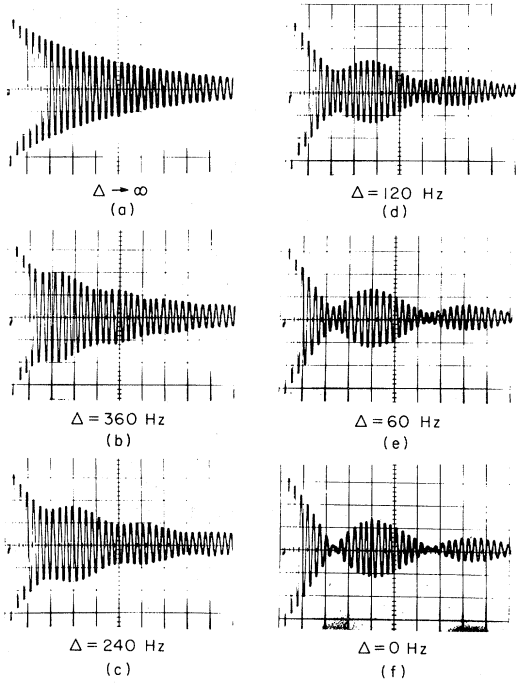

FIG. 3. Similar to Fig. 2 but with the proton transition stimulated at a fixed power level with the indicated frequency offsets, Δ. Time scale: 1 msec/division.

$$D_4 = (\sin\theta/8A)\, e^{-\Gamma t}\,[(A+\Delta)\cos\tfrac{1}{2}(A-\Delta-2\delta)t + (A-\Delta)\cos\tfrac{1}{2}(A+\Delta+2\delta)t\,], \tag{36}$$

where

$$A = (\Delta^2+X^2)^{1/2}.$$

From Eq. (28), the radiated power is proportional to $D_3^2+D_4^2$. This power is eventually observed as a voltage

$$V \propto (D_3^2+D_4^2)^{1/2} \equiv S(t,\Delta). \tag{37}$$

Forming this magnitude from Eq. (36) gives the relatively simple result

$$S(t,\Delta) = \tfrac{1}{4}\sin\theta\, e^{-\Gamma t}\,[1-(X^2/A^2)\sin^2(\tfrac{1}{2}At)]^{1/2}. \tag{38}$$

The voltage function $S(t)$ has the character of a modulated decaying exponential. Note that if the proton transition is not stimulated (i.e., $X=0$) then we have the simple exponential decay characteristic of free electron precession. If the proton transition is stimulated at resonance ($\Delta=0$), then $A=X$ and

$$S(t,0) = \tfrac{1}{4}\sin\theta\, e^{-\Gamma t}\,\left|\cos\tfrac{1}{2}Xt\right|. \tag{39}$$

The result is pure sinusoidal modulation with nodes at $t=\pi/X,\ 3\pi/X,\ 5\pi/X,\ \ldots$. The rf field parameter X may be measured by observing the nodal separation. A number of these double-resonance signals at different rf power levels are shown in

Fig. 2.

If the proton driving field is slightly off resonance, Eq. (38) indicates that there will be a modulation of the exponential with period $2\pi/A$ but that the nodes will not be sharp. For a given value of X, the modulation becomes more rapid and decreases in amplitude as $|\Delta|$ increases. This behavior is illustrated in Fig. 3.

The physics of this situation is easily visualized if we remember that each of the atomic states is in fact a product state of proton and electron spin states. The initial pulse rotates the electronic component of state (2) into a precessing superposition of states (2) and (3). The proton state is unaffected by this change. Stimulating the transition (1-2) gradually rotates the proton component of the precessing state to state (1) and back again. The electron state is unaffected by this latter rotation, and thus keeps its phase, but atoms which "find themselves" in state (1) can no longer radiate at the (2-3) frequency. This uniform rotation between proton states produces a sinusoidal modulation of the free-precession signal.

3. *Line Shape in Low-Flux Operation*

The voltage function $S(t)$ represents the output signal for given values of X and Δ. From this we must determine the proton resonance frequency Ω_0 by comparing the output signals for a range of known input frequencies Ω. (Recall that $\Delta = \Omega - \Omega_0$.) A straightforward procedure is to evaluate the time integral of $S(t)$ as a function of Ω; since the basic behavior is exponential decay, this is in effect obtaining the Laplace transform of the modulation of the decay envelope caused by double resonance.

For purposes of analysis it is most convenient to carry out the integration over the interval $0 \le t < \infty$. In practice, of course, one must introduce a finite upper limit to the observation period. The slight correction to the idealized line shape caused by this will be treated later.

The observed signal is proportional to

$$U(\Delta) = \int_0^\infty S(t, \Delta)\, dt = \frac{\sin\theta}{4} \int_0^\infty e^{-\Gamma t} \left[1 - \left(\frac{X}{A}\right)^2 \sin^2 \frac{At}{2} \right]^{1/2} dt \,. \tag{40}$$

We expand the integrand in a power series:

$$U(\Delta) = \frac{\sin\theta}{4} \int_0^\infty e^{-\Gamma t} \left[1 - \frac{1}{2}\left(\frac{X}{A}\right)^2 \sin^2 \frac{At}{2} - \frac{1}{2^2 2!}(X/A)^4 \sin^4 \frac{At}{2} - \cdots \right.$$
$$\left. - \frac{(1)(3)(5)\cdots(2n-3)}{2^n n!} \left(\frac{X}{A}\right)^{2n} \sin^{2n} \frac{At}{2} - \cdots \right] dt \,. \tag{41}$$

This can be integrated termwise to give

$$U(\Delta) = \frac{\sin\theta}{4\Gamma} \left(1 - \frac{1}{4} \frac{X^2}{\Gamma^2 + A^2} - \frac{4!}{2^6 2!} \frac{X^4}{[\Gamma^2 + A^2][\Gamma^2 + (2A)^2]} - \cdots \right.$$
$$\left. - \frac{[(1)(3)(5)\cdots(2n-3)](2n)!}{2^{3n} n!} \frac{X^{2n}}{[\Gamma^2 + A^2][\Gamma^2 + (2A)^2]\cdots[\Gamma^2 + (nA)^2]} - \cdots \right) \,. \tag{42}$$

The series converges absolutely and uniformly. The first term, which is independent of Δ, represents the signal due to pure exponential decay observed when the proton transition is not stimulated ($X = 0$). The second term—let us call it U_2—is pure Lorentzian,

$$U_2(\Delta) \approx \frac{X^2}{\Delta^2 + X^2 + \Gamma^2} \,, \tag{43}$$

centered at $\Delta = 0$, with half-width $(\Gamma^2 + X^2)^{1/2}$. The higher-order terms cause a weak distortion in the Lorentzian. Note, however, that these terms are even functions of Δ, and hence $U(\Delta)$ is symmetric about $\Delta = 0$; the resonance line is slightly narrowed but it is not shifted. The worst distortions occur when $X \gg \Gamma$, in which case $U_3/U_2 \approx 3/16$. The line shape continues to be very nearly Lorentzian even for large values of X.

To compare the theoretical and experimental line shapes, the line shape has been calculated numerically for a finite integration period, $T_i < t < T_f$, corresponding to the experimental observation time. For practical reasons an offset frequency ν_a is introduced experimentally in the electron signal (this is illustrated in Figs. 2 and 3) and the signal is rectified to obtain the decay envelope. The corresponding theoretical expression for the resonance line is

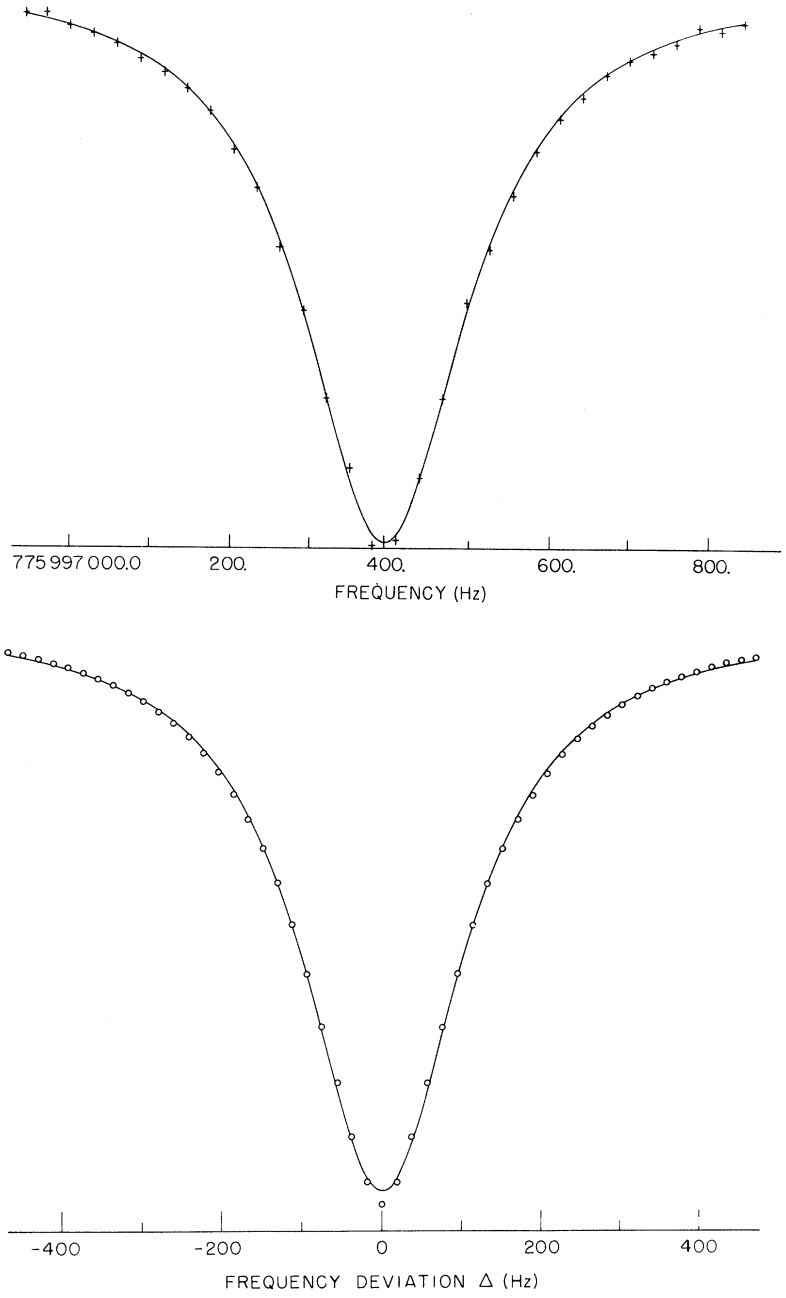

FIG. 4. Comparison of experimental data (upper curve) with the theoretical line shape, Eq. (44) (lower curve). The solid line is the best-fit Lorentzian curve.

$$U'(\Delta) = \int_{T_i}^{T_f} |S(t, \Delta)| \, |\sin 2\pi\nu_a t| \, dt \ . \tag{44}$$

[$S(t, \Delta)$ is again given by Eq. (38).] $U'(\Delta)$ is compared with the experimental line shape in Fig. 4. The continuous curve in each figure is the best Lorentzian fit to each set of points.

D. Behavior at High Flux

1. *Numerical Solution for Arbitrary Flux*

Although the low-flux solution describes the important features of our double-resonance system, it is not adequate to account for effects due to nonlinearities such as the observed variation in decay rate with the length of the microwave pulse at high-flux levels.

We return to the general rate equations (27) with α and β given by Eqs. (22) and (26). By numerical integration, solutions to the equations were obtained for given values of X, Δ, flux, and other input parameters. These yielded exact values for the voltage function $S(t, \Delta)$ and the integrated signal function

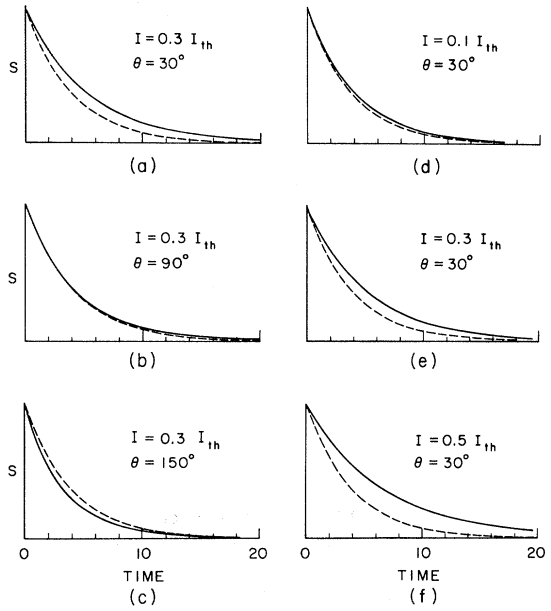

FIG. 5. Computed value of electron free-precession signals. The dashed curve is the expected result in the absence of radiation damping. Time in milliseconds.

$$U'(\Delta) = \int_{T_i}^{T_f} S(t, \Delta)\, dt \ .$$

To obtain a theoretical double-resonance line, numerical solutions of the rate equations and integration of the transient signals were carried out for a range of proton frequency offsets Δ, giving a set of points $U_i' = U'(\Delta_i)$. This is analogous to an experimental sweep, which similarly gives the integrated amplitude at discrete frequency points. Thus we have, in effect, a computer model for the experiment. Fitting the best Lorentzian curve to the computer-model points by a least-squares technique enables us to study frequency shifts and linewidth as a function of various experimental parameters.

2. *Nonlinear Effects*

Numerical integration of the rate equations at low-atomic-flux levels gives solutions which are essentially the same as the exact solutions to the simplified equations in the low-flux limit. However, as the flux approaches the threshold level, behavior of the system begins to deviate from the simple solutions, as one would expect. Since the important features of this high-flux behavior do not involve double resonance, we can take $X = 0$ in the following discussion, corresponding to simple exponential decay in the low-flux limit

$$S(t)_{\text{low flux}} = \tfrac{1}{4}\sin\theta\, e^{-\Gamma t} \ . \qquad (45)$$

In the intermediate flux range ($I/I_{th} \approx 0.1$–0.5), we find that the decay remains close to exponential but that the decay rate varies with the pulse width θ. The apparent decay rate Γ' is greater than Γ if θ is less than 90°, and vice versa. This phenomenon can be explained in terms of radiation damping.[11] Consider again the vector magnetization model. The effect of the pulse is to rotate the magnetization $\vec{M}$, originally aligned with the static field $\vec{H}_0$, through a polar angle θ. $\vec{M}$ precesses about $\vec{H}_0$ at a frequency ω_0 and radiates power $P \propto \sin^2\theta$. Gradually the magnetization relaxes owing to loss of atoms and to dephasing, but at low-flux levels θ remains approximately constant. If the atomic density is large, however, the power radiated stimulates further polar rotation of $\vec{M}$ relative to $\vec{H}_0$, so that θ gradually increases after the initial pulse. Thus the radiated power changes not only because of relaxation, but also because of the increase in θ. For $\theta < 90°$, $\sin^2\theta$ and P start to increase in time, effectively increasing Γ, while for $\theta > 90°$ the effect is to suppress P and produce a decrease in Γ. For $\theta \sim 90°$, $\sin^2\theta$ is stationary for small changes in θ, and $\Gamma' \approx \Gamma$. This behavior is shown in Fig. 5, where numerical solutions for $S(t)$ at various flux levels and pulse lengths are plotted. The corresponding solution $S(t)_{\text{low flux}}$ is shown for comparison.

This dependence of decay rate on pulse width has been observed experimentally by operating the maser at maximum flux. The observed decay rates are compared with theory in Fig. 6. The results indicate that the flux at the time of the measurement was about $0.4 I_{th}$, in agreement with estimates based on the initial signal amplitude. (This measurement was made under high-flux conditions which could not be maintained over an extended period of time because of pumping system limitations.)

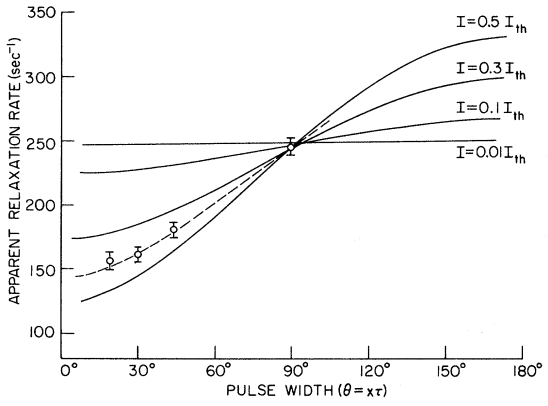

FIG. 6. Apparent relaxation rate as a function of beam flux and pulse width—comparison of theory and experiment.

The radiation damping effect has also been investigated, both theoretically and experimentally, under double-resonance conditions ($X>0$). These investigations showed no observable variation of the proton resonance frequency associated with radiation damping, and only very small (less than 1%) variation in the proton linewidth. Thus there is no effect on the g-factor ratio determination.

3. *Effect of Cavity Mistuning*

A more important effect for the g-factor ratio measurement arises from mistuning of the microwave cavity. Unlike the nonlinear effects associated with radiation damping, cavity mistuning introduces errors into the measurement of resonance frequencies for both the electron and proton transitions. In the case of stationary oscillation the effect on the radiating (2-3) transition is well known.[10] The fractional shift in the oscillation frequency ω is given by

$$\frac{\omega-\omega_0}{\omega_0}=\frac{(\omega_c-\omega_0)}{\omega_0}\frac{Q_c}{Q_L}\ , \tag{46}$$

where ω_0 is the electron resonance frequency, and ω_c is the cavity frequency. Q_c and Q_L are quality factors for the cavity and resonance line, respectively.

The situation is quite different below threshold. It can be shown[12] that in this case

$$\frac{\omega-\omega_0}{\omega_0}=\frac{\omega_c-\omega_0}{\omega_0}\frac{Q_c}{Q_L}\left(\frac{2I}{I_{\rm th}}\mathcal{P}\right)\ , \tag{47}$$

where I is the flux of atoms to the cavity, $I_{\rm th}$ is the threshold flux, and $\mathcal{P}$ is the instantaneous polarization. $\mathcal{P}$ varies in time because of atomic flow and radiation effects, so that the frequency shift is nonstationary. The observed shift depends on both the preparation of the system and the interval during which the frequency is measured. Nevertheless, it is always smaller than in the case of stationary oscillation. Since Q_c/Q_L is typically 10^{-4}, even a gross mistuning of the cavity by 0.1 MHz (out of a 1-MHz cavity width) produces a fractional shift in the electron resonance of $\approx 10^{-9}$, which is a negligible source of error.

The proton transition both complicates the analysis and enhances the cavity pulling effect. Essentially, the proton transition is coupled to the electron transition by their common level, and a shift in one produces an opposite shift in the other. Because the g-factor ratio is 25 times more sensitive to errors in the proton frequency than to errors in the electron frequency, the indirect effect of cavity pulling on the proton transition dominates. To calculate the size of the effect we numerically integrated the rate equations [Eqs. (27)] using various values of the phase angle φ [Eq. (23)]. The proton resonance lines were found to be shifted by

$$\Delta_m=\Omega_m-\Omega_0\propto-\frac{Q_c}{Q_L}(\omega_c-\omega_0)\frac{I}{I_{\rm th}}\ . \tag{48}$$

At a typical flux level $I=0.2I_{\rm th}$, mistuning the cavity by 10% of its width shifts the proton resonance by approximately 1% of the proton linewidth. This is an important effect, resulting in a fractional error in the g-factor ratio of $\delta R/R\approx 7\times10^{-8}$. Shifts of this magnitude have been observed by purposely mistuning the cavity. The effect is sufficiently large to require care in keeping the cavity properly tuned. Fortunately, as described in Sec. IV, the cavity can readily be tuned to 1% of its width (i.e., to 10 kHz) so that the maximum effect on a g-factor determination is less than 7 parts in 10^9.

E. Field-Averaging Effects

We have already noted that the dominant relaxation mechanism for the radiating electron moment is dephasing as the atoms move randomly through an inhomogeneous static field. In Eq. (14) we assumed that the result is simple relaxation of the form

$$\dot{\rho}_{23}=-(1/\tau_2)\rho_{23}\ , \tag{49}$$

resulting in a pure exponential decay. Brenner[13] has shown that this is not necessarily so, and that motion through nonuniform fields can cause frequency shifts in addition to relaxation. Such shifts, which we shall call "inhomogeneity shifts," are important in our experiment. By applying Brenner's methods to our three-level system, we shall see that the electron frequency is shifted slightly but that once again the important effect for the g-factor ratio measurement is an indirect shift in the proton transition due to its coupling to the electron system.

Inhomogeneity shifts arise from a variety of effects. One of the most important cases occurs when random motion through an inhomogeneous field produces an asymmetric distribution of phases of the atomic moments about a reference vector in quadrature with the oscillating field. If the static field were uniform, all the moments would lie along the reference vector. A nonzero component of the oscillating moment orthogonal to this vector is equivalent to a frequency shift. The average phase is, by definition, $\langle\delta\rangle=0$. However, the orthogonal component is given by $\langle\sin\delta\rangle$, and for an asymmetric distribution of phase this will not be zero. The resulting shift is likely to be important if there is a small spatial region of extreme field value, especially if the geometry is such that the small region communicates poorly with the rest of the system. The stem of the maser storage bulb is just such a small, relative-

ly isolated region, and the field value is extreme there.

Brenner has also pointed out that frequency shifts result when two volumes are somehow "weighted." For instance, if the effective relaxation is different in the two regions, then a phase shift received in one region does not have the same influence as a phase shift received in the other. This effect is primarily responsible for frequency shifts in the present experiment.

In our three-level system the electron transition is strongly field dependent, and field inhomogeneities account for most of the electron linewidth. Associated inhomogeneity shifts in the electron frequency may occur, but, as we shall see, they play a negligible role in the absence of double-resonance stimulation ($X=0$). Suppose now that the proton transition is stimulated by an rf field which is strong in the bulb region, which we denote by a, and weak in the small stem region b. We can think of the double resonance as a "competition" between proton and electron transitions: Strong stimulation of the proton transition removes atoms rapidly from the radiating state, giving a weak electron oscillating moment, and *vice versa*. Hence, the strong proton rf field behaves like a source of increased relaxation in region a, and the contribution from that region to the total oscillating magnetization is decreased relative to the contribution from region b. If the average static field differs in the two regions, the electron resonance is shifted toward the value in b.

In practice, the inhomogeneity shift in the electron frequency in our experiment is rather insignificant: no more than about 5 Hz, or 5 parts in 10^{10}. However, as already described, the proton and electron resonances are coupled by their common level. A shift $\delta\omega$ in the electron line produces a shift $\delta\Omega$ in the proton line which is proportional to the relative widths of the lines. If we denote the electron and proton half-widths by $\Delta\omega$ and $\Delta\Omega$, respectively, the shifts are related by

$$\delta\Omega \approx \delta\omega\, \Delta\Omega/\Delta\omega \ . \tag{50}$$

This can produce a shift in the proton resonance as large as a few Hz, which corresponds to an error in R of several parts in 10^7.

We investigated the inhomogeneity shift by following Brenner's procedure of subdividing the system and solving the density-matrix equations for each subvolume. The subvolumes are coupled by simple flow rates. Our model consists of two volumes: a large volume a, corresponding to the main body of the storage bulb, and a small volume b, corresponding to the stem region. The static fields are constant in each volume but differ by an amount ΔH_0, so that the electron resonance frequencies differ by $\delta_0 = \gamma \Delta H_0$. Rate equations for this model are derived in Appendix A. Here we summarize the results based on numerical integration of these equations.

If we let $w = N_b/N_a$, where N_b and N_a are the number of radiating atoms in each region, then the electron resonance line, which is close to Lorentzian, decays with a transverse relaxation rate

$$(1/\tau_2) \cong 0.7\, w^2 \delta_0^2 \tau \ . \tag{51}$$

(A similar result, with a slightly different numerical coefficient, is also predicted by Brenner's steady-state theory.)

The inhomogeneity broadening is also accompanied by a shift $\delta\omega$ in the resonance line. Our results for this shift can be most easily interpreted from a result of Brenner[13] using his steady-state theory:

$$\delta\omega = -(1/\tau)(w\tau\delta_0)^3 + 2\delta_0 w^2 \tau(\Gamma_a - \Gamma_b) \ , \tag{52}$$

where Γ_a and Γ_b are effective average relaxation rates in the two volumes due to escape of atoms from the system and "quenching" of the oscillating moment when the proton resonance is stimulated. In Brenner's application the first term dominated, whereas in the present case the second term dominates. Equation (41) suggests that we take Γ_a and Γ_b to be of the form

$$\Gamma_a = (\Gamma^2 + X_a^2)^{1/2} \ , \quad \Gamma_b = (\Gamma^2 + X_b^2)^{1/2} \ , \tag{53}$$

where X_a and X_b are the amplitudes of the field (in reduced units) driving the proton transitions in the two volumes. At all but the lowest levels of radiation fields used experimentally we can take $\Gamma_a \approx X_a$, $\Gamma_b \approx X_b$, in which case the electron frequency shift may be written as

$$\delta\omega = 2\delta_0 w^2 \tau(1 - X_b/X_a)\, \Gamma_a \ . \tag{54}$$

If we equate Γ_a with $\Delta\Omega$, the observed proton half-width, then Eqs. (50) and (54) yield

$$\delta\Omega = C\delta_0 w^2 \tau\, (1 - X_b/X_a)\, \Delta\Omega^2/\Delta\omega \ . \tag{55}$$

C is an undetermined constant of proportionality expected to be of order unity. This result provides insight into the dependence of the proton shift on the rf field distribution, magnetic field gradients, and the electron and proton linewidths. The proton linewidth is a particularly important parameter since it is the only one which can be freely varied in the experiment. The fact that Eq. (55) does not provide the numerical coefficient is of little consequence in view of the fact that the model is at best an approximation, and in any case it is impossible to evaluate experimentally all the important parameters, particularly the field gradients.

To verify Eq. (55) we numerically integrated the rate equations described in Appendix A using

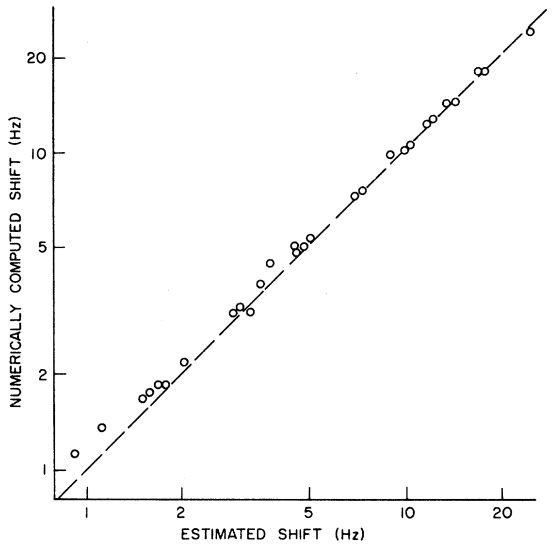

FIG. 7. Numerical results for shift in proton resonance due to inhomogeneity effect versus value estimated with Eq. (55).

values for the field gradients and storage volumes which are reasonable for our experimental conditions. One test that these choices are indeed realistic is that the calculated and observed linewidths agree closely. The results for the proton frequency shift are well described by Eq. (55) with $C = 2.5$. A plot of the numerical results for $\delta\Omega$ versus the expression in Eq. (55) is shown in Fig. 7. The scatter in points is due to rounding errors in the computations. The slight departure from Eq. (55) at small linewidths can be ascribed to breakdown of the approximation that $X > \Gamma$ which was introduced in Eq. (54). If this approximation is dropped, one would expect that at lowest linewidths $\delta\omega$ would vary with $\Delta\Omega$ less rapidly than quadratically, which is suggested by the numerical results shown in Fig. 7.

The symmetry of the resonance line is also important. Unlike the steady-state, single-resonance case treated by Brenner, where no distortions of the resonance line occur, we find that small asymmetries accompany the inhomogeneity shifts in our system. These have also been observed experimentally. The slightly asymmetric lines can be fit extremely well by allowing a dispersive component to the Lorentzian line shape in the least-squares fit process. In all cases the dispersion amplitude is less than 5% of that for absorption. Figure 8 shows an experimental resonance line observed when large field distortions were present and fit by a Lorentzian with a dispersive component. A comparable theoretical line obtained from numerical integration of the two-region model is also displayed.

F. Consideration of the (2-3-4) Double-Resonance System

Up to this point all our work has dealt with the double-resonance system consisting of levels (1), (2), and (3) of Fig. 1. Experimentally we also observe the second proton resonance (3-4). We shall see that no modifications at all are necessary in our treatment if we simply reinterpret the previous rate equations (27) in a rather obvious way.

We develop the new rate equations exactly as we did in Sec. II B 3. If we let

$$\begin{aligned} \mathcal{O}_1 &= \rho_{33} - \rho_{44} , \\ \mathcal{O}_2 &= \rho_{22} - \rho_{33} , \\ \rho_{34} &= (D_1 + iD_2)\, e^{-i\Omega t} , \\ \rho_{23} &= (D_3 + iD_4)\, e^{-i\omega t} , \\ \rho_{24} &= -(D_5 + iD_6)\, e^{-i(\Omega+\omega)t} , \end{aligned} \tag{56}$$

we recover a set of equations identical to Eq. (27).

Since both double-resonance systems are described by the same equations with the same initial conditions, their behavior is identical. All the analysis up to this point applies equally well to either system. This is an invaluable advantage when we consider the two most worrisome sources of frequency shift—cavity mistuning and field inhomogeneity—both of which shift the two transitions in the same direction. Since $\nu_{p1} + \nu_{p2} = \nu_0$, where ν_0 is the hyperfine frequency, any unidirectional shift in both ν_{p1} and ν_{p2} will manifest itself as an incorrect observed value for ν_0. Thus if ν_0, as determined from our experiment, agrees with the accepted value within statistical limits, we can rule out the possibility of significant systematic error resulting from the above effects. This is particularly important in the case of inhomogeneity shifts, where we must extrapolate with a semi-empirical relationship to remove the shift.

An alternative and completely equivalent test is to look for a difference in the g-factor ratio R as determined from ν_{p1} and ν_{p2}. An upward shift in ν_{p1} increases R; the same shift in ν_{p2} decreases R. Thus, the absence of a statistically significant difference between the two determinations of R can also place a limit on systematic errors due to unidirectional shifts.

G. Effect of Spin Exchange

Spin exchange provides another mechanism which can alter the states of atoms in the maser. It can lead to both relaxation and a frequency shift. This phenomenon has been discussed theoretically by numerous authors[7,14] and the effect has been measured and utilized in hydrogen maser research.[15] In Appendix B we outline the development for the strong-field case. The spin-exchange terms to be added to the density-matrix rate equations are given

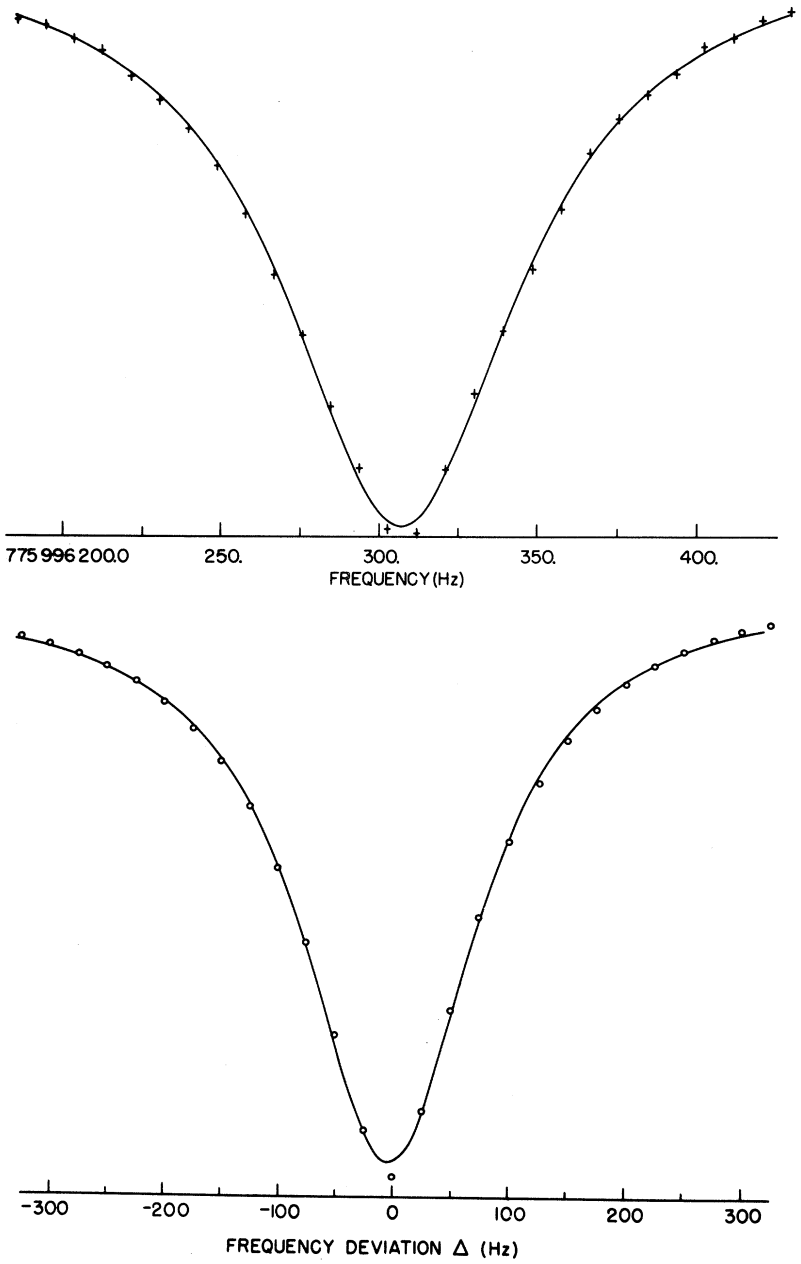

FIG. 8. Comparison of experimental data under conditions of high line asymmetry due to the inhomogeneity shift (upper curve) with data computed numerically from the two-region model (lower curve). The solid line is the best-fit Lorentzian curve with a dispersive component.

in Eqs. (B9). For either the (1-2-3) or (2-3-4) system we need keep only the three off-diagonal elements which are coupled by the radiation field. As usual these are broken into real and imaginary parts, so with the four diagonal elements ten equations are necessary to describe either system. The rate equations for $D_1, \ldots, D_6$, the real and imaginary parts of the off-diagonal elements, are obtained by adding the spin-exchange terms (B9) to Eqs. (27). For the (1-2-3) system the results are

system we need keep only the three off-diagonal elements which are coupled by the radiation field. As usual these are broken into real and imaginary parts, so with the four diagonal elements ten equations are necessary to describe either system. The rate equations for $D_1, \ldots, D_6$, the real and imaginary parts of the off-diagonal elements, are obtained by adding the spin-exchange terms (B9) to Eqs. (27). For the (1-2-3) system the results are

$$\rho_{11} = -\gamma\rho_{11} - XD_2 + \tfrac{1}{2}\gamma - U(\rho_{11}\rho_{33} - \rho_{22}\rho_{44}) ,$$

$$\rho_{22} = -\gamma\rho_{22} + XD_2 - 2K(\alpha D_4 - \beta D_3) + \tfrac{1}{2}\gamma + U(\rho_{11}\rho_{33} - \rho_{22}\rho_{44}) ,$$

$$\rho_{33} = -\gamma\rho_{33} + 2K(\alpha D_4 - \beta D_3) - U(\rho_{11}\rho_{33} - \rho_{22}\rho_{44}) ,$$

$$\rho_{44} = -\gamma\rho_{44} + U(\rho_{11}\rho_{33} - \rho_{22}\rho_{44}) ,$$
$$D_1 = -\gamma D_1 - \Delta D_2 + K(\beta D_5 - \alpha D_6) - U(\rho_{33} + \rho_{44}) D_1 + V(D_4 D_5 - D_3 D_6) , \quad (57)$$
$$\vdots$$

where

$$U = n\langle v_{rel}\rangle \sigma_{ex}, \quad V = \kappa n \langle v_{rel}\rangle \sigma_{ex} . \quad (58)$$

n is the density: $n = I/\gamma V_b$. σ_{ex} is the spin-exchange cross section and κ is the shift parameter. A similar set of equations governs the system (2-3-4), the only difference being an opposite sign for two nonlinear spin-exchange terms.

Equations (57) have been numerically integrated, using the values for σ_{ex} and κ given in Appendix B. The resonance lines are symmetric in shape with frequency shifts which are positive and equal to within 1% for the two proton transitions. The magnitude of the shift at a typical flux level of $0.2 I_{th}$ is predicted to be 0.3 Hz, which is equivalent to a fractional shift of 2×10^{-8} in the g-factor ratio. However, just as in the case of cavity pulling and inhomogeneity shifts, the effect of spin exchange on R is equal and opposite for the two proton transitions, and in principle it need not introduce any systematic error into the g-factor ratio measurement.

H. Resonance Shifts Due to Nonresonant Fields

We have so far neglected the effect of nonresonant terms on the evolution of the density matrix. The counter-rotating component of a linearly polarized field can give rise to the Bloch-Siegert effect, and related shifts occur due to the influence of the proton driving signal on the electron resonance, and vice versa. All of these effects are described by a formula due to Ramsey[16]:

$$\delta\omega = \tfrac{1}{2} X^2/(\omega_0 - \omega_2) . \quad (59)$$

X is the perturbing matrix element in frequency units, ω_2 is the frequency of the nonresonant field, and ω_0 is the unperturbed resonance frequency.

The largest shifts are due to the proton driving signal. In this case, $X \sim 200$ rad/sec and $\omega_0 \sim 4\times10^9$ rad/sec. The Bloch-Siegert effect is found by taking $\omega_2 = -\omega_0$. This gives a fractional shift in the proton frequency of 1 part in 10^{15}, entirely negligible. Since $\omega_e \gg \Omega_p$, the effect of the proton signal on the electron frequency is even smaller, and it, too, can be neglected.

III. APPARATUS

A. Design Considerations

The atomic-hydrogen maser used in our experiment is similar to a conventional (21 cm) hydrogen maser,[17] except that the cavity and storage bulb are located within the gap of a 3500 G magnet and are reduced in size for operation at a wavelength of 3 cm. The design is illustrated schematically in Fig. 9. Molecular hydrogen is dissociated in a discharge tube and effuses into a vacuum to form an atomic beam. The beam passes through a magnetic state selector which focuses atoms in the states (1) and (2) (Fig. 1) into a Teflon-coated storage bulb located in a cavity tuned to the electron resonance. The maser operates below threshold for continuous oscillation, and the atoms are prepared in a radiating state by application of a $\frac{1}{2}\pi$ pulse at the electron transition frequency. The radiated signal is detected by conventional means. The proton transition is driven by a single turn loop located in the cavity.

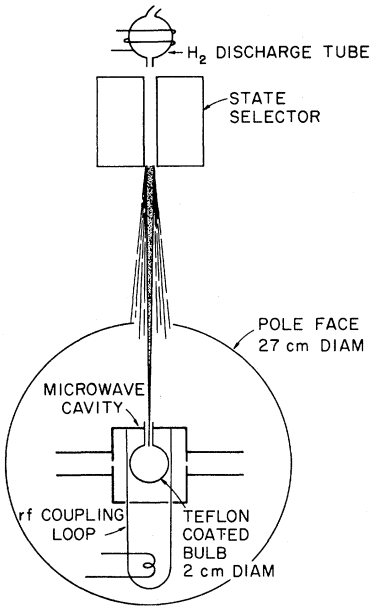

FIG. 9. Schematic diagram of the apparatus.

Selection of a field strength involved balancing several considerations: (1) Higher fields provide greater sensitivity as the proton-applied field interaction becomes larger relative to the hyperfine interaction. (2) The electron transition frequency ν_e increases linearly with field strength, requiring a decrease in size for the resonance cavity and storage bulb. Such a decrease reduces both the atomic flux into the bulb and the geometric lifetime, resulting in a loss of sensitivity. (3) For a given fractional field homogeneity, relaxation due to atomic dephasing in the field gradients becomes increasingly worse as the field is increased, as indicated by Eq. (14). A further consideration is that the magnetic field must have a fractional stability comparable with the electron linewidth. A field of 3500 G, provided by a permanent mag-

net, was chosen as a reasonable compromise taking into account all these considerations.

B. Magnet

A permanent magnet was selected because of its high intrinsic stability and because the field gradients are relatively constant; once the gradients have been minimized by careful mechanical shimming, little further attention is necessary for several months. (In contrast, an electromagnet requires reshimming whenever the current is altered. Superconducting magnets which might also fulfill our criteria were not available when the apparatus was designed.) The magnet was designed and built by the Mullard Radio Valve Company, Surrey, England. Its specifications are: Field strength: 3525 G at 35 °C. Adjustable ± 0.1% by mechanical shunts. Homogeneity: About 2.5×10^{-7} peak deviation over 2-cm-diam spherical volume (optimum). Temperature coefficient: − 250 ppm per 1 °C, with a time constant of about 4 days. Dimensions: Pole gap, 26.6 cm diam × 6.5 cm wide; magnet yoke (box shaped), 76 × 72 × 41 cm. Over-all size (including thermal insulation): 112 × 103 × 86 cm. Mass: 880 kg.

Provision is made for shimming through mechanical adjustment of the pole faces for parallelism and lateral alignment. Nineteen electromagnetic shims enable fine adjustment of the field for optimum homogeneity. For the purposes of shimming, the maser is removed and a 0.05-cm^3-water NMR probe is used to map the field. The field is swept with a sawtooth of amplitude $\Delta H/H \approx 5 \times 10^{-8}$. The NMR signal is sharp enough to resolve field differences of 5×10^{-8}. The probe is moved about the sample region by a precision tridirectional manipulator. The complete shimming of the field is a long and tedious exercise. Fortunately the gradients are quite stable; once properly shimmed, only occasional fine electrical adjustments are necessary. These can be made with the maser in place by observing the electron free-precession signal and maximizing the decay lifetime. Particularly convenient for such fine adjustments are a set of "orthogonal" electromagnetic shims designed on the principle of a Legendre polynomial expansion of the field in rectangular coordinates.[18] These shims are reasonably independent in effect and enable the gradients to be adjusted without shifting the average field. The optimum homogeneity as measured by the NMR probe is a rms deviation of about 1 part in 10^7 over the sample volume (a 2-cm-diam sphere) with a maximum deviation of less than 3 parts in 10^7.

The temperature coefficient of the magnetic field is high (250 ppm per 1 °C) and extremely precise temperature regulation is necessary. The yoke region of the magnet is thermally isolated. The gap is maintained at 35 °C by continuous introduction of warm air whose temperature is regulated by a high-gain servo system. This system readily keeps the field stable to 1×10^{-7} over a period of 1 h, and to 2 ppm over several days.

To minimize mechanical vibrations, the entire magnet assembly is "floated" on air cushions which have a resonance frequency of approximately 1 Hz. This mechanical isolation substantially reduces noise on the signal due to field jitter and preserves the mechanical shimming adjustment. A counterweighted elevator raises the maser assembly out of the magnet gap for adjustments. When in place the maser rests firmly on the magnet assembly and is disconnected from the elevator, so that the entire system is mechanically isolated.

Residual noise in the field appears to be due to a combination of pickup of stray 60-Hz fields (the magnet only shields these by a factor of about 10) and microphonic effects. The fractional fluctuations are about 10^{-8}, comparable with the electron linewidth. Fortunately, the detection system described below is insensitive to these fluctuations.

C. Maser

1. *Source Assembly and Vacuum System*

The source uses an rf dissociator and the state selector is a hexapole magnet; both are of conventional design.[17]

The source vacuum chamber is a 15-cm-diam stainless-steel cylinder with the state-selector magnet mounted on the axis, as shown in Fig. 10. The source bulb is mounted in a short T section off the main chamber, with a steel bellows arrangement to permit alignment when the system is under vacuum. The bottom of the source chamber connects to a glass tube which supports the cavity and storage bulb. The source chamber and storage bulb can be isolated by a ball valve in order to permit changing storage bulbs without letting the entire system up to air.

The vacuum pump is an NRC model 206 Orb-Ion pump, rated at 800 l/sec for air at high vacuum, which pumps by titanium gettering plus ionization of rare gases by circulating electrons. It is 15 cm in diameter and is mounted vertically above the source chamber. The system achieves a vacuum of 10^{-8} Torr with no load. The source chamber pressure is typically 1×10^{-5} when the maser is operating. At this pressure pumping speed deteriorates markedly after 4–6 h of continuous running, but is regenerated after a rest period of approximately 24 h.

2. *Microwave Cavity and* rf *Coupling Loop*

The microwave cavity is cylindrical, (4-cm inner diameter) and operates in the TE_{011} mode. The

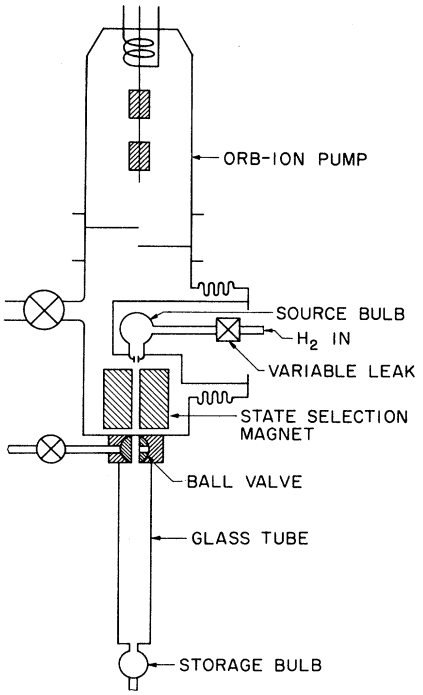

FIG. 10. Schematic diagram of vacuum system.

length can be varied from 3.5 to 5.3 cm. Considerable leeway for adjustment is necessary because different storage bulbs change the loading drastically. The cavity is made of thin beryllium-copper in order to minimize field distortions due to diamagnetism. The magnetic properties of the cavity assembly were carefully checked by NMR at various stages of machining. The cavity has a polished silver surface and a loaded Q of about 10 000. Microwave signals are coupled through small holes leading to waveguides on opposite sides of the cylinder.

The storage bulb stem makes a vacuum seal to the upper end plate by means of an O-ring and sleeve. The cavity and bulb are in turn attached to the vacuum system by a pyrex glass cylinder 40 cm long×3-cm inner diameter which extends from the state selector down into the magnet gap. Glass is used to minimize eddy-current effects. For the same reason, the waveguide sections extending into the magnet are made of silver-plated Plexiglass. The assembled cavity and rf coupling loop are illustrated in Fig. 11.

The rf field that stimulates the proton transition is supplied by a coupling loop consisting of two parallel wires running the length of the cavity. To avoid degrading the cavity Q through mode distortion, the wires are drawn taut perpendicular to the microwave electric field. Power is coupled into the loop inductively. The loop is sufficiently broadbanded to allow coupling of power at either 644 or 776 MHz.

3. *Storage Bulb*

The storage bulb is a thin sphere of fused quartz with an entrance stem and a second dummy stem opposite for alignment, as shown in Fig. 11. All bulbs are coated with DuPont FEP-120 Teflon by the following procedure: The bulb is cleaned with a mixture of nitric and hydrofluoric acids, and then rinsed with distilled water. The Teflon suspension is sloshed over the entire surface and the bulb is drained in an inverted position and then dried with a gentle stream of dry nitrogen. The bulb is then baked at 375 °C for 1 h with a stream of dry air flowing through it.

For a spherical bulb of volume V_B the geometric lifetime (mean time an atom spends in the bulb) is given by[17]

$$\tau_g = 3\,\frac{l}{d}\,\frac{V_B}{A}\,\frac{1}{\langle v\rangle}\ . \tag{60}$$

V_B is the volume of the bulb, A is the area of the entrance aperture, l/d is the length-diameter ratio for the stem, and $\langle v\rangle$ is the mean atomic speed. The flux to the bulb varies almost linearly with A.

As discussed in Sec. IV D, the signal-to-noise ratio is improved by increasing τ_g and/or the atomic flux. In order to achieve a long lifetime without shrinking the entrance aperture, a collimator is placed in the bulb stem. The collimator is simply a few pieces of thin-walled Teflon spaghetti tubing packed into the stem and extending into the bulb, as shown in Fig. 11. The dimensions of a typical bulb are: Bulb diameter: 21 mm; wall thickness: 0.25–0.5 mm; stem length: 24 mm; inner diameter: 3 mm; outer diameter: 5 mm; collimator: two tubes, 19×1.1-mm inner diameter. The geometric lifetime for this bulb is calculated at 14 msec. This is in good agreement with the longitudinal relaxation time of 12.8 msec as measured by the method discussed in Sec. IV D.

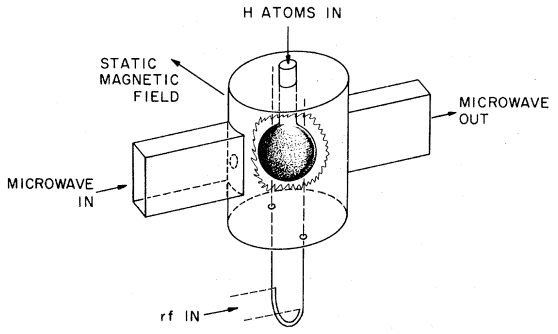

FIG. 11. Cavity and storage bulb.

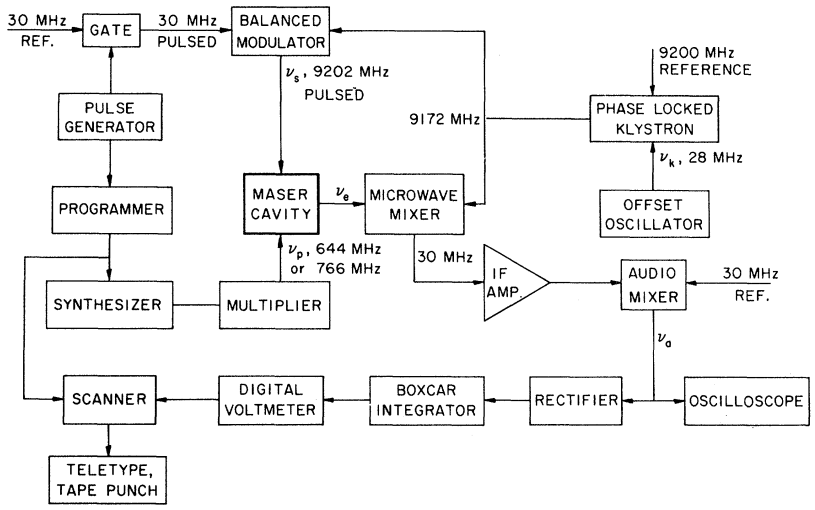

FIG. 12. Signal processing system.

D. Electronics

The electron and proton transitions are stimulated by coherently generated sources, and the electron signal is coherently detected. The system for accomplishing these tasks is shown in Fig. 12.

The primary frequency reference is a Sulzer 2.5 C crystal oscillator which is continually monitored against the NBS WWVB frequency reference broadcase; 30- and 9200-MHz reference signals are generated by frequency multiplication. against the NBS WWVB frequency reference broadcast; 30- and 9200-MHz reference signals are generated by frequency multiplication.

A klystron is phase locked to the 9200-MHz reference signal via an offset signal ν_k generated by a Hewlett-Packard (HP) 606B signal generator which is stablilized by a HP 8708A synchronizer. ν_k is monitored by a HP 5245L frequency counter. The microwave stimulating pulses are generated by mixing a 30-MHz sideband from a pulsed gate with the klystron signal. The frequency of the resulting signal is

$$\nu_s = 9230 \text{ MHz} - \nu_k \ . \tag{61}$$

ν_k lies within the range 28-29 MHz, so that $9201 \leq \nu_s \leq 9202$ MHz. This range is adequate for matching ν_s to the electron frequency ν_e over the possible excursions in magnetic field due to temperature variations or the exigencies of shimming.

The radiated free-precession signal is mixed and amplified, as shown in Fig. 12, and converted to an audio signal at frequency ν_a:

$$\nu_a = \nu_s - \nu_e = 9230 \text{ MHz} - (\nu_e + \nu_k) \ . \tag{62}$$

At this point the signal has the form

$$S_a(t, \Delta) = S(t, \Delta) \sin(2\pi\nu_a t + \varphi_a) \ , \tag{63}$$

where φ_a is an unimportant phase factor which we henceforth neglect, and $S(t, \Delta)$ is the amplitude of the free-precession signal as given by Eq. (38). The bandwidth of the audio mixer is limited by a simple RC filter with a bandwidth of 14 kHz. The signal-to-noise ratio is sufficiently high that the free-precession signal is readily monitored on an oscilloscope.

The audio signal is accurately rectified by a circuit which is linear over a 60-dB range, and the output is integrated by a PAR Model CW-1 boxcar integrator. The output of the boxcar has the form

$$U(\Delta) = \langle \int_{T_i}^{T_f} |S_a(t, \Delta)| dt \rangle$$

$$= \langle \int |S(t, \Delta)| \, |\sin(2\pi\nu_a t)| dt \rangle \ . \tag{64}$$

Here T_i and T_f are limits of the boxcar "window" and the brackets indicate the time average dictated by the time constant of the boxcar integrator. $U(\Delta)$ is referred to as the "integrated amplitude." Its theoretical counterpart $U'(\Delta)$ was discussed in Secs. II C and II D. An important feature of this detection system is that the bandwidth is so large that the effect of small field fluctuations on the audio signal is negligible as long as ν_a is greater than a few kHz.

The proton driving signal at frequency ν_p, is provided by adding the output of a HP 5100A frequency synthesizer to a multiple of 100 MHz from the frequency standard, and using the output to drive a Gertsch FM-4A phase-locked oscillator.

The entire system is controlled by a digital programmer which periodically halts the system to record $U(\Delta)$ and the proton applied frequency ν_p' on a teletype, sets the proton frequency to a new value according to a preset pattern, and restores the system to operation. Data reduction is done by computer from the teletype's punched tape output.

IV. EXPERIMENTAL PROCEDURE

A. Early Experiments

Preliminary results obtained in a preceding experiment have been reported previously.[1] At that time the proton resonance frequency was measured by adjusting the frequency of the applied rf field for maximum modulation of the free-precession decay signal [e.g., Fig. 3(f)] as observed on an oscilliscope. The accuracy was limited by inability to display the double-resonance line shape and to search for small systematic errors such as those due to the effects of field inhomogeneity. Nevertheless, this relatively crude detection method gave a value of R with a fractional uncertainty of 3×10^{-7}.

Before adopting the method described here we attempted using cw, rather than pulsed, detection. A small microwave signal was fed continuously into the microwave cavity and was amplified by the electron resonance. By stimulating the proton transition the gain of the maser was modified. For this technique to be successful the magnetic field must be sufficiently stable that short term jitter is small compared to the electron linewidth; this requires an instantaneous field stability of 1 part in 10^8 or better. The observed jitter was generally several times larger than this. Attempts to lock the field to the electron line center by various modulation and feedback schemes were not successful owing to the broad spectrum of field fluctuations. Since the cw method is not inherently more sensitive than the pulsed method finally adopted, the attempt was dropped.

B. Pulse Integration Technique

The observation method selected involves measuring the effect on the decay envelope of the electron free-precession signal by a continuously applied rf field at the proton frequency. As described in Sec. III D, each datum consists of the output signal of the boxcar integrator for a selected value of the proton frequency:

$$U(\Delta) = \langle \int_{T_i}^{T_f} |S(t, \Delta)| \, |\sin 2\pi \nu_\alpha t| \, dt \rangle \, . \tag{64}$$

The boxcar window is opened at time T_i approximately 0.5 msec after the termination of the $\frac{1}{2}\pi$ microwave pulse. (This value, and those that follow in this description, are typical; in practice there were variations of up to 50% in the indicated times.) The window length $T_f - T_i$ is 10 msec (2 decay lifetimes) and the signal is repeated with a period of 20 msec. The time constant of the boxcar is 0.1 sec and the total sampling period is 2 sec of which 1 sec represents actual gate time. At the end of each sampling period, the output signal of the boxcar integrator, $U(\Delta)$, and the value of the applied proton frequency, ν_p', are digitally recorded as a datum. The proton frequency is set to a new value and the whole process is repeated.

A "sweep" of the proton line consists of a series of 20–40 such data at equally spaced intervals approximately symmetric about the line center.

C. Experimental Procedure

The following steps constitute a typical "run" consisting of one night's observations:

(i) Preliminaries. Magnetic field gradient coils are adjusted to give maximum electron lifetime and the field is trimmed until electron resonance and cavity resonance coincide.

(ii) Data taking. (a) The rf power level is adjusted to give desired proton linewidth. The time between nodes in decay envelope at resonance is read from oscilloscope display. (b) The proton resonance center is estimated visually. (c) The synthesizer control is programmed for symmetric sweep over the proton resonance. Sweep width is typically 3 full (3 dB) linewidths. (d) The electron frequency ν_e is measured by adjusting klystron offset frequency ν_k for zero audio beat, as observed visually on oscilloscope. (e) ν_k is offset to produce 2-kHz audio note ν_a. (f) The line sweep commences. The line is swept in the directions of increasing and decreasing frequency, with klystron set above and below ν_e by the audio offset ν_a, for a total of four sweeps. Step (d) is repeated after every pair of sweeps. (g) Steps (a)–(f) are repeated with new values of the rf power.

While each sweep is in progress the electron signal is visually monitored on the oscilloscope and the field trim coil is continually adjusted to hold the audio-signal-frequency constant. By this method the field can be maintained indefinitely within 1×10^{-8} of its initial value. At occasional intervals during a run the cavity resonance is monitored and, if drift has occurred, the field is trimmed to the new cavity frequency. This can be done to an accuracy of 2 kHz, and the cavity resonance and the field are kept in coincidence to within 10 kHz.

The four sweeps of the proton line are analyzed together to average out distortions due to the finite sweep speed and slight asymmetries in the detection system. We refer to a set of four such sweeps as a symmetrized group. An evening's run consists of 10–25 symmetrized groups. Ideally, data are taken on both proton transitions during one run. In practice, this was achieved only occasionally.

The data are subsequently analyzed to yield values for ν_p and R by methods described in Sec. V. The data of a typical run are shown in Table I. In addition to these numerical results, the data for each group are plotted by computer along with the best-fit curve in order to allow visual inspection of all

TABLE I. Typical experimental data—three symmetrized groups at different rf power levels. $1/\Gamma = 4.9$ msec.

Electron frequency (Hz)	Proton frequency (Hz)	Half-width (Hz)	g-factor ratio (error)
Group 1: rf attenuation = − 8 dB, first node at $t = 11.5$ msec			
9 201 186 014.0	775 996 707.34	47.1	658.210 638 (13)
6014.0	06.98	48.3	0 655 (14)
6031.0	06.82	48.0	0 659 (14)
6031.0	06.72	47.2	0 663 (13)
			0 654 (07)
Group 2: rf attenuation = − 4 dB, first node at $t = 7.4$ msec			
6419	07.08	65.7	0 585 (19)
6419	06.30	66.0	0 620 (18)
6466	05.78	67.2	0 636 (21)
6466	05.44	66.9	0 651 (21)
			0 623 (10)
Group 3: rf attenuation = − 0 dB, first node at $t = 4.4$ msec			
6867	07.48	94.8	0 497 (26)
6867	08.54	96.3	0 450 (34)
6773	06.85	95.4	0 540 (27)
6773	06.70	97.5	0 546 (26)
			0 508 (14)

the data. An example of this graphical output is shown in Fig. 4.

D. Signal-to-Noise Ratio

The signal-to-noise ratio (S/N) establishes the statistical resolution of the experiment. For this reason, and to establish that operation of the apparatus is well understood, it is important to show that the observed S/N is in reasonable agreement with the predicted value. We shall separately consider the S/N for the electron free-precession signal $(S/N)_e$ and for the proton resonance $(S/N)_p$.

1. *Electron Signal-to-Noise Ratio*

Let I be the total flux of atoms entering the storage bulb. The power radiated at the electron frequency is given by Eq. (28) which yields the following expression in the absence of double resonance and with correct cavity tuning:

$$P_{\text{rad}} = (Ih\nu_e K/8\gamma)\, e^{-2\Gamma t} \ . \tag{65}$$

The observed signal power P_s is smaller than P_{rad} by a factor $\beta/(1+\beta)$, where β is the coupling coefficient. By combining Eqs. (65) and (24), we obtain the following expression for P_s^0, the signal power at $t = 0$:

$$P_s^0 = \frac{\beta}{1+\beta}\, \frac{\pi^2 g_s^2 \mu_B^2 Q \pi \nu_e}{8\gamma^2 V_c}\, I^2 \ . \tag{66}$$

The expression becomes somewhat simpler if we introduce the threshold flux for oscillation I_{th}, given by Eq. (30):

$$P_s^0 = \frac{\Gamma}{4\gamma}\, \frac{\beta}{1+\beta}\, \frac{I^2}{I_{\text{th}}}\, h\nu \ . \tag{67}$$

(Note that this result holds only for $I < I_{\text{th}}$.) The following values are typical:

$$Q = 10^4, \qquad \gamma = 80 \text{ sec}^{-1},$$
$$\beta = 1, \qquad \Gamma = 250 \text{ sec}^{-1},$$
$$\eta = 3, \qquad \nu = 9.2 \times 10^9 \text{ Hz},$$
$$V_c = 60 \text{ cm}^3, \qquad I = 1.5 \times 10^{13} \text{ atoms sec}^{-1} .$$

Substitution into Eqs. (30) and (67) gives

$$I_{\text{th}} = 8 \times 10^{13} \text{ atoms sec}^{-1},$$
$$P_s^0 = 7 \times 10^{-12} \text{ W} .$$

This is typical of the observed signal power, although accurate confirmation is lacking because of the difficulty of calibrating the gain of the detection system. Furthermore, the beam flux, which is estimated from the observed effects of radiation damping (Sec. II D), is known only approximately.

For a detection system of bandwidth $\Delta\nu$ and noise figure F, the noise power P_n is

$$P_n = kT\Delta\nu F \ . \tag{68}$$

The noise figure F is established by the microwave-mixer preamp. The bandwidth is limited by the final-audio-amplifier rectifier which has a variable low-pass filter normally set at 14 kHz (3 dB point). At $T = 300\,^\circ$K and with $F = 8$ dB, the noise power is $P_n = 4.6 \times 10^{-16}$ W, for a voltage signal-to-noise ratio of

$$(S/N)_e = (P_s^0/kT\Delta\nu F)^{1/2} = 120 \ . \tag{69}$$

The observed S/N is in the range 60–100, in reasonable agreement with the predicted value. Field jitter may account for the excess noise.

2. *Proton Signal-to-Noise*

The proton signal-to-noise ratio is closely related to $(S/N)_e$. The integrated modulation amplitude is given by Eq. (64). Since the observed signal is actually a rectified sine wave, rather than the dc envelope, the amplitude is reduced by a factor of $2/\pi$. Since the finite gate time T_g is generally long compared to Γ^{-1}, the upper limit in the integral can be taken to be infinity with little error. We can express the integrated amplitude as a voltage in terms of the initial electron power P_s^0 and power gain G referenced to a resistance R. We divide by the integration time T_g to obtain the average observed voltage:

$$\langle V(\Delta)\rangle = \frac{2}{\pi}\,(GRP_s^0)^{1/2}\,\frac{1}{\Gamma T_g}\left(1-\frac{1}{4}\,\frac{X^2}{\Gamma^2+X^2+\Delta^2}\right) . \tag{70}$$

The effective proton-signal amplitude is

$$S_p = \langle V(\infty)\rangle - \langle V(0)\rangle = \frac{1}{2\pi\Gamma T_g}\,(GRP_s^0)^{1/2}\,\frac{X^2}{\Gamma^2+X^2} . \tag{71}$$

The corresponding noise voltage is obtained from Eq. (68) with the bandwidth determined by the boxcar integrator time constant $\tau = 1/\pi(\Delta\nu)_p$:

$$N_p = (GRkTF/\pi\tau)^{1/2} . \tag{72}$$

Combining Eqs. (69), (71), and (72) we obtain the effective signal-to-noise ratio for the proton line:

$$\left(\frac{S}{N}\right)_p = \left(\frac{S}{N}\right)_e \left(\frac{\tau\Delta\nu}{4\pi}\right)^{1/2} \frac{1}{\Gamma T_g}\,\frac{X^2}{\Gamma^2+X^2} . \tag{73}$$

For all but the lowest values of the rf field $X \gtrsim 2\Gamma$, and we can neglect the Γ^2 term in the denominator. If we substitute the previous numerical values into Eq. (73) along with $\tau = 0.1$ sec, $T_g = 12$ msec, we obtain

$$(S/N) = 400 .$$

The observed signal-to-noise in a corresponding experimental case, as measured by taking the ratio of the amplitude at the center of the proton line to its standard deviation, is typically 80–150. Field jitter again probably accounts for the excess observed noise.

E. Relaxation Rate and Linewidth

The atomic polarization relaxes by flow processes at a rate $1/\tau_g$, where τ_g is the "geometrical lifetime" in the bulb, while the oscillating moment relaxes at a rate $\Gamma = 1/\tau_g + \gamma_2$, where $\gamma_2 = 1/\tau_2$ is the relaxation rate due to the effect of field inhomogeneities. In this section we compare the measured and predicted relaxation rates for the electron and proton transitions.

1. *Geometric Lifetime*

The geometric lifetime can be measured by observing the time needed for $\mathcal{P}_2$, the polarization which drives the electron transition, to return to equilibrium after it has been upset by a microwave pulse.

Consider the case where the electron polarization is periodically driven by a short resonant pulse which precesses the magnetization through angle θ. The interval between pulses is T, and we assume that $1/T \ll 1/\tau_g + 1/\tau_2$, so that the magnetization effectively decays to zero between pulses. If $\mathcal{P}_2^i$ is the polarization at the start of the pulse, then it can be shown from Eq. (27) that its value at the end of the pulse is

$$\mathcal{P}_2^f = \mathcal{P}_2^i \cos\theta . \tag{74}$$

The polarization then relaxes to the initial value

$$\mathcal{P}_2^i = \tfrac{1}{2} + (\mathcal{P}_2^f - \tfrac{1}{2})\,e^{-T/\tau_g} . \tag{75}$$

It follows that

$$\mathcal{P}_2^i = \frac{1}{2}\left(\frac{1-e^{-T/\tau_g}}{1-e^{-T/\tau_g}\cos\theta}\right). \tag{76}$$

The signal amplitude immediately after the pulse is given by

$$S_0 \propto \mathcal{P}_2^i \sin\theta . \tag{77}$$

If we denote the amplitude for $T \gg \tau_g$ by $S_0(\infty)$, we have

$$e^{-T/\tau_g} = \frac{S_0(\infty) - S_0(T)}{S_0(\infty) - S_0(T)\cos\theta} . \tag{78}$$

Normally θ is chosen to be $\frac{1}{2}\pi$. τ_g is found by measuring $S_0(T)$ for several values of T. Values obtained are quite consistent and generally agree with the calculated lifetimes to 10%.

2. *Electron Linewidth*

The radiating moment decays as $e^{-\Gamma t}$, where

$$\Gamma = 1/\tau_2 + 1/\tau_g . \tag{79}$$

Γ is readily determined from visual observation of the electron signal on an oscilloscope, and τ_g is known both from the geometry of the bulb and from the measurement procedure just described. Thus, the transverse relaxation rate τ_2^{-1} is also known.

There are two mechanisms which contribute to τ_2^{-1}. The first is due to random motion through the residual gradients of the storage bulb. From Eq. (14) we have

$$\tau_{2b}^{-1} \approx \langle \delta^2 \rangle \tau_c , \tag{80}$$

where $\langle\delta^2\rangle = \gamma_{23}^2 \langle \Delta H^2 \rangle_b$ is the variance of the electron resonance frequency over the spherical storage bulb, and τ_c is the mean time between collisions. Gas collisions are negligible, so τ_c is given by[17] $\tau_c = 2D/3\langle v \rangle$, where $\langle v \rangle$ is the mean atomic speed and D is the diameter of the storage bulb. $\langle\delta^2\rangle$ is calculated from a mapping of the magnetic field by NMR. Under optimum conditions the field varies quadratically from the center of the bulb with a maximum deviation of 2.5 parts in 10^7. This gives an rms inhomogeneity of 0.7×10^{-7}. Using $\gamma_{23} = 1.76\times10^7$ rad sec^{-1} G^{-1}, $D=2$ cm, and $\langle v \rangle = 2.5 \times10^5$ cm sec^{-1}, we obtain $\tau_{2b}^{-1} \approx 100$ sec^{-1}.

The second contribution to τ_2 arises from the effect of trapping of the atoms in the stem of the storage bulb. This is given by Sec. II D, Eq. (51), which can be written as

$$\tau_{2s}^{-1} = 0.7 w^2 \delta_s^2 / S \ , \tag{81}$$

where δ_s is the difference in mean electron frequency between the stem and the rest of the bulb, w is the ratio of neck volume to bulb volume, and S is the rate at which flow occurs from the bulb to the neck. w and S are set by the geometry of the bulb; typical values are $w = 0.015$, $S = 800$ sec^{-1}. The field difference is estimated by mapping the sample region with a small NMR probe. The fields typically differ by 3 parts in 10^7, although it should be pointed out that this estimate is necessarily crude since the mapping is not done with the bulb present, and diamagnetic effects of the bulb and cavity can be significant. The predicted value is $\tau_{2s}^{-1} \approx 100$ sec^{-1}.

The total transverse relaxation rate is

$$\tau_2^{-1} = \tau_{2s}^{-1} + \tau_{2b}^{-1} \approx 200 \text{ sec}^{-1} \ . \tag{82}$$

Typically, the electron decay lifetime is 5 msec with $\tau_g = 15$ msec. From Eq. (79) these yield $\tau_2^{-1} = 130$ sec^{-1}, somewhat less than our estimate but in good agreement considering the difficulty of estimating the field gradients. In any case, the approximate agreement between observed and calculated lifetimes gives confidence that there is no major undiscovered source of relaxation.

3. *Proton Linewidth*

Unlike the electron linewidth, the proton linewidth can be predicted to high accuracy. From Eq. (42) it is seen that in the low flux limit the proton resonance line is approximately Lorentzian with a linewidth of $2(\Gamma^2 + X^2)^{1/2}$. Γ is found by direct observation of the electron decay rate, and X is determined by measuring the time between nodes in the electron signal when the proton transition is driven at resonance, Fig. 2. From Eq. (39) we have

$$X = 2\pi / T_n \ , \tag{83}$$

where T_n is the time between nodes. The proton linewidth can be found from a panoramic display of the proton line, Fig. 4, and is also provided as one of the output parameters in the curve-fitting procedure described in Sec. IV F. The observed and predicted linewidths agree within the experimental resolution of a few percent, providing the detailed theoretical lineshape, Eq. (44), is used.

F. Curve-Fitting Procedure

It was shown in Sec. II that the expected lineshape is Lorentzian, to first order. At low power levels the correction terms of Eq. (42) are negligible. With increased power the higher order terms of Eq. (42) are appreciable, but a pure Lorentzian still gives a good fit with no error in the line center and no more than a few percent error in the linewidth. This conclusion still holds when the effect of the finite gate time of the boxcar integrator is included. Consequently, in the absence of a closed form representation for Eq. (44), we have chosen to fit our data with a Lorentzian curve.

The data $(U(\nu_p'), \nu_p')$ are fitted to a pure Lorentzian by a straightforward iterative curve-fitting program. Each sweep of 40 points extending over 3 full linewidths is reduced independently. The output data consist of four parameters (baseline, amplitude, center frequency, and linewidth) as well as a computer generated plot of the best-fitting curve superimposed upon the data, Fig. 4. In addition, the program calculates σ_p, the standard deviation of the center frequency ν_p, as follows.

Let $L(\nu)$ represent the Lorentzian curve which is fitted to the data $(U(\nu_j), \nu_j)$; $j = 1, \ldots, N$. Assuming that all of the points depart from $L(\nu)$ as independent random variables, the variance is given by

$$S^2 = \frac{1}{N-4} \sum_{j=1}^{N} (U(\nu_j) - L(\nu_j))^2 \ . \tag{84}$$

The standard deviation of the center frequency ν_p is given by

$$\sigma_p = S \left[\sum_{j=1}^{N} \left(\frac{\partial \nu_p}{\partial U(\nu_j)} \right)^2 \right]^{1/2} \ . \tag{85}$$

The derivatives $\partial\nu_p / \partial U(\nu_j)$ are found by numerically varying each value of $U(\nu_j)$ by a small amount, 5% of the amplitude of L, and recalculating the value of ν_p.

V. RESULTS AND INTERPRETATION

Interpretation of the results of this experiment involves the usual complexities and value judgments which characterize high precision measurements. As we shall see, the pivotal problem lies in understanding the frequency shifts due to motional averaging effects. To set the stage for this problem, let us first examine the role of purely statis-

tical errors.

A. Statistical Error

The standard deviation σ_R in R due to errors in ν_p, ν_c, and ν_0 is

$$\frac{\sigma_R}{R}=\frac{1}{R}\left[\left(\nu_p\frac{\partial R}{\partial\nu_p}\right)^2\left(\frac{\sigma_p}{\nu_p}\right)^2+\left(\nu_e\frac{\partial R}{\partial\nu_e}\right)^2\left(\frac{\sigma_e}{\nu_e}\right)^2+\left(\nu_0\frac{\partial R}{\partial\nu_0}\right)^2\left(\frac{\sigma_0}{\nu_0}\right)^2\right]^{1/2}, \quad (86)$$

where σ_p, σ_e, and σ_0 are standard deviations for ν_p, ν_e and ν_0, respectively. From Eqs. (7) and (8) we obtain the following results for the fractional error in R at our operating field. For measurements made with proton transition 1,

$$\frac{\sigma_R}{R}=\left[\left(43\frac{\sigma_{p1}}{\nu_{p1}}\right)^2+\left(2.2\frac{\sigma_e}{\nu_e}\right)^2+\left(41\frac{\sigma_0}{\nu_0}\right)^2\right]^{1/2}, \quad (87a)$$

and for measurements made with proton transition 2,

$$\frac{\sigma_R}{R}=\left[\left(52\frac{\sigma_{p2}}{\nu_{p2}}\right)^2+\left(2.2\frac{\sigma_e}{\nu_e}\right)^2+\left(54\frac{\sigma_0}{\nu_0}\right)^2\right]^{1/2}. \quad (87b)$$

The errors in ν_p, ν_e, and ν_0 are assumed to be uncorrelated. (A number of errors involving ν_p and ν_e are, in fact, correlated. However, these are essentially nonstatistical in origin, and will be treated separately in following sections.) The hyperfine frequency is accurately known[19] and its uncertainty $\sigma_0/\nu_0=1.4\times10^{-12}$ introduces negligible error in R.

The standard deviation of an individual determination of ν_e is taken to be $\sigma_e=60$ Hz, the typical standard deviation for successive measurements made with the procedure described in Sec. IV C.

The standard deviation in ν_p is obtained from the curve fitting routine described in Sec. IV E. For a single sweep of the proton line the value for σ_p is seldom less than 0.3 Hz, with values up to 1.5 Hz occuring for broad lines. Substituting $\sigma_p=0.3$ Hz and $\sigma_e=60$ Hz into Eq. (86) yields

$$\sigma_R/R=(4.1+2.0)^{1/2}\times10^{-8}=2.5\times10^{-8}, \quad (88)$$

with the dominant contribution from σ_p. Thus the primary contribution to σ_R in a single sweep is uncertainty in the proton frequency. Values for the standard deviation in R calculated this way are in good agreement with the measured standard deviation of successive identical sweeps of the proton line.

All line sweeps are carried out in groups of four, as previously described, and the best value of ν_p is found from

$$\nu_p=\tfrac{1}{4}\sum_{n=1}^{4}\nu_p(n), \quad (89)$$

where $\nu_p(n)$ is the value of a particular sweep. (An unweighted average is used in order to preserve the symmetry of the contribution from each sweep.) The standard deviation of the mean is taken to be

$$\sigma_p^2=\tfrac{1}{16}\sum_{n=1}^{4}\sigma_p(n)^2. \quad (90)$$

B. Nonstatistical Errors

1. *Shifts Due to Motional Field Averaging*

The most prominent systematic error in this experiment is a result of the frequency shifts associated with motional averaging effects. Equation (55) indicates that the shift in ν_p, the proton frequency, is proportional to the square of the proton linewidth, which suggests that the experiment be repeated at different values of proton linewidth and the results be extrapolated to zero linewidth. Since the validity of the extrapolation procedure is of critical importance, two somewhat different methods were used to analyze the data.

Method 1: *Quadratic extrapolation.* Equation (55) suggests that the shift in the proton resonance frequency is proportional to the square of $\Delta\nu_p$, the proton half-width. This result is essentially empirical; its justification lies in its agreement with numerical results from integration of the equations of motion (Fig. 7). Over the region for which Eq. (55) is valid we expect that the true value of the g-factor ratio is related to the apparent value R by

$$R'=R+k\Delta\nu_p^2, \quad (91)$$

where k is an unknown factor which depends on the magnetic field gradients and storage bulb geometry.

Equation (91) requires that the experimental values for R' be extrapolated to $\Delta\nu_p=0$ in order to eliminate the inhomogeneity shifts. To test this procedure, which we shall call the quadratic extrapolation procedure, the equations of motion for the two-region model developed in Appendix A were integrated to yield $S(t,\Delta)$ and the integrated amplitude $U'(\Delta)$ [Eq. (44)] for various values of Δ. These points were then treated as raw data which were reduced by the procedure described. The resulting values of R were extrapolated to zero proton linewidth according to Eq. (91). The results are shown in Fig. 13. The gradients were assigned to give shifts in R and a value of τ_2 close to those observed. The two curves correspond to results for the two proton transitions (1-2) and (3-4). The quadratic extrapolation is reasonably good, though there is a residual error in R of about 1 part in 10^8. This is not unexpected; as indicated in Fig. 7, slight departures from simple

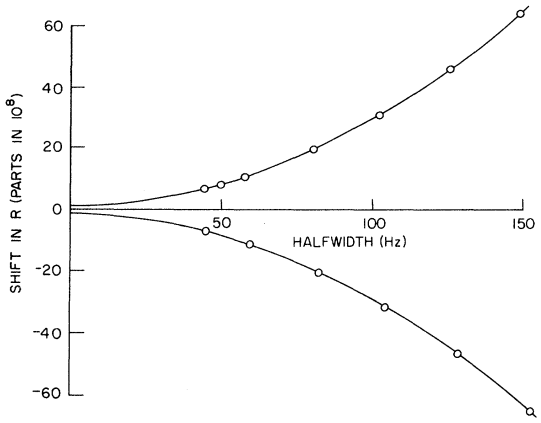

FIG. 13. Computed values of the change in R due to inhomogeneity shift versus proton half-width. The upper and lower curves correspond to proton transitions 1 and 2, respectively. The solid lines are the best-fit quadratic curve.

quadratic shifts are present at narrow linewidths.

Plots of experimental values of R versus $\Delta\nu_p$ for three different runs are shown in Fig. 14. Although inhomogeneity shifts of several parts in 10^7 are evident, the extrapolated values are consistent to within a few parts in 10^8.

It appears that the quadratic extrapolation procedure can lead to a small residual error in any single determination of R. However, the sign of the error differs for measurements made on the two proton transitions ν_{p1} and ν_{p2}, so that the remaining error should be eliminated by averaging

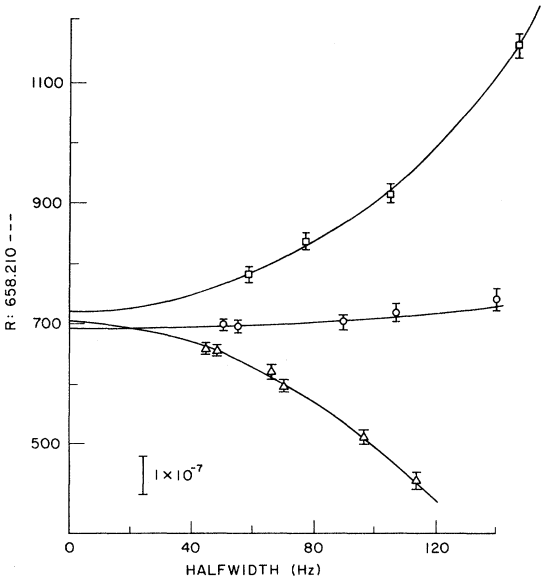

FIG. 14. R versus proton half-width for measurements made with three different applied gradients. The solid lines are the best-fit quadratic curves.

measurements made in succession on ν_{p1} and ν_{p2}. On only three runs were data on both proton transitions obtained. Results for these runs are shown in Table II. If we denote results for ν_{p1} by R_1 and results for ν_{p2} by R_2, we see that the sign and magnitude of $R_1 - R_2$ differ from run to run.

The question remains as to whether the residual error introduced by the quadratic extrapolation method is correlated between runs. If it is, then averaging values of R_1 and R_2 should eliminate it. If the error is uncorrelated, then it can change in sign and its effect will be to increase the variance of R from run to run. In either case, the quadratic extrapolation method should not introduce a source of systematic error.

We should note that the situation is not improved by introducing a linear term in the quadratic extrapolation formula. The quadratic terms dominate over the experimentally accessible region, and attempts to fit a linear term without *a priori* knowledge of its magnitude seriously degrades the goodness of fit.

Results for R, with the data extrapolated quadratically, are shown in Fig. 15. These data were not edited; all results for a series of 19 runs are included. The only data rejected were from runs in which operating conditions were intentionally distorted to search for systematic shifts.

Method 2: *Linear extrapolation with dispersive line shape*. As pointed out in Sec. II E, inhomogeneity shift can produce both a displacement of the resonance line and a distortion. The distortion is small and is well described by a dispersive component to the Lorentzian line. This suggests that at least a portion of the apparent shift can be removed by fitting the data to a Lorentzian curve with a dispersive component. To test this, the numerically generated data which were used to test the quadratic extrapolation method, Fig. 13, were also fitted to Lorentzian-plus-dispersion curves. The results are shown in Fig. 16. The residual shift in R is small and is linear in proton linewidth. The remaining error in R when the results are extrapolated to zero linewidth is well under one part in 10^8. Data from three experimental runs analyzed by the linear extrapolation method are shown in Fig. 17. Residual errors appear to be beneath the limit of experimental resolution.

TABLE II. Comparison of R_1 and R_2 for measurements made under similar conditions. Errors are 1 standard deviation.

Run	R_1	R_2	$\frac{1}{2}(R_1+R_2)$	$\frac{1}{2}(R_1-R_2)$
1	658.210 671(31)	658.210 700(6)	658.210 685(16)	−0.000 029(32)
2	658.210 714(9)	658.210 699(5)	658.210 706(5)	+0.000 015(10)
3	658.210 720(10)	658.210 701(6)	658.210 710(6)	+0.000 020(12)

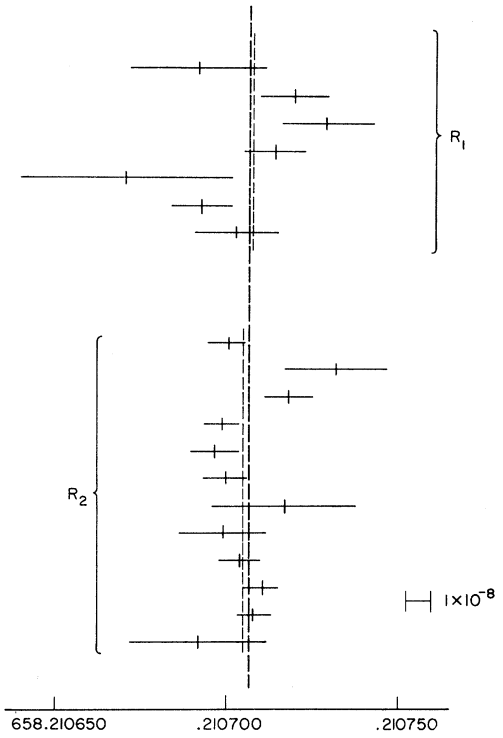

FIG. 15. Complete data summary of results for R as analyzed by the method of quadratic extrapolation. The mean value and mean for each group are indicated by vertical dashed lines.

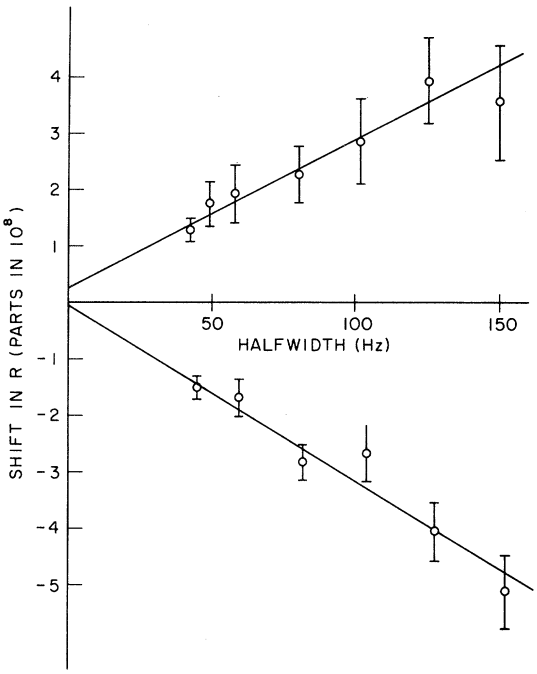

FIG. 16. Computed values for change in R due to inhomogeneity shift versus proton half-width. The points correspond to the same computer-generated data as in Fig. 13, but a dispersive component has been added to the Lorentzian curve. (Error bars are estimated computer error.)

The entire collection of data for R was analyzed by this method, which we shall refer to simply as the linear extrapolation method. The results are shown in Fig. 18. Curiously, the scatter with this method is more than twice as large as that with the quadratic extrapolation method. We have not been able to find the explanation for this.

The results for both methods of analysis are summarized in Table III. The data for both transitions are summarized separately. For reasons to be discussed, the final values of R are the unweighted averages of R_1 and R_2. The results of Table III show that the values of R found by the two extrapolation procedures differ by far less than the experimental error. Although the agreement may be fortuitous, it helps to give confidence in the extrapolation procedures.

2. *Other Nonstatistical Errors*

(*a*) *Spin exchange*. The effect of spin exchange is discussed in Sec. II G and Appendix B. At a typical flux level of $I = 0.2 I_{th}$ spin exchange should cause a shift in R of 2×10^{-8}. The sign of the shift is opposite for the two proton transitions, R_1 being shifted upwards and R_2 downwards. Consequently, the average value, $R = \frac{1}{2}(R_1 + R_2)$ is unaffected by spin exchange. However, spin exchange should manifest itself in a difference between measurements for the two transitions: $(R_1 - R_2)/R = 4 \times 10^{-8}$. The results shown in Table III indicate no such discrepancy. R_1 and R_2 agree within the statistical error, less than 1×10^{-8}, and the sign of the difference is in fact opposite with the two extrapolation procedures. Two possible ex-

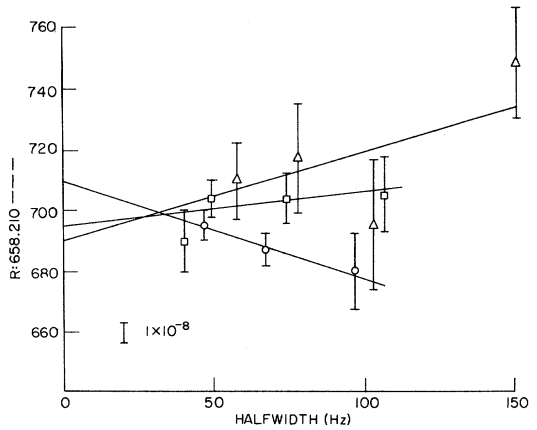

FIG. 17. Typical values for R versus proton half-width for data fitted to a dispersive curve. The solid lines are the best-fit straight lines.

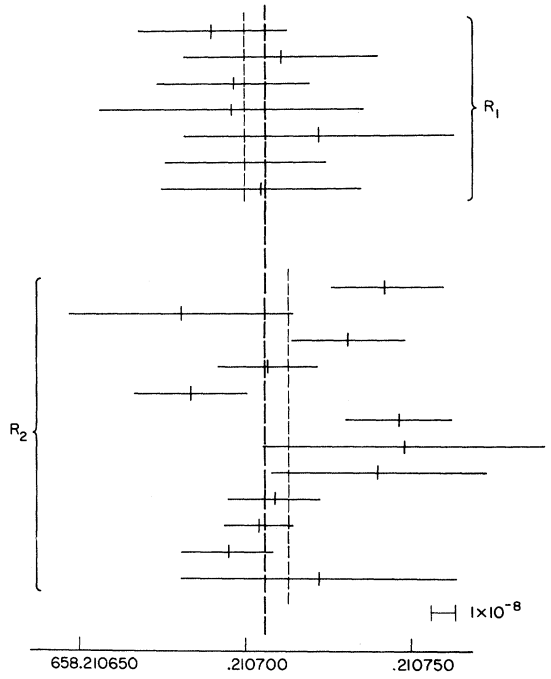

FIG. 18. Complete data summary of results for R as analyzed by the method of dispersive fit with linear extrapolation. The mean value and mean for each group are indicated by vertical dashed lines.

planations for the absence of spin-exchange effects are that the flux may be lower than assumed or that the spin-exchange shift may be masked by an anomalously high wall shift.

(*b*) *Wall shift.* Collisions with the wall of the storage bulb cause a change in the hyperfine frequency given by

$$\delta\nu_0 = \varphi/2\pi\tau_c \,, \tag{92}$$

where φ is a phase shift characteristic of the wall material and τ_c^{-1} is the collision rate. For FEP Teflon the phase shift has been found by Zitzewitz[20] to be -8.2×10^{-6} rad. The mean collision rate is readily found from the bulb geometry. For the bulb described in Sec. III B the result is $\delta\nu_0 = -0.24$ Hz.

The effect of the wall shift on R is to decrease R_1 by 7×10^{-9} and to increase R_2 by the same amount. The average of R_1 and R_2 is unaffected. The changes in R_1 and R_2 due to the wall shift are smaller than those due to spin exchange, and of opposite sign. However, as discussed above, there is no experimentally resolvable difference between the two values of R.

(*c*) *Systematic line asymmetry.* As has been noted, line asymmetries of several percent can occur because of the field-inhomogeneity effect. Presumably their effect is eliminated by the extrapolation procedures. There is, however, the possibility that a small systematic asymmetry may result from some unknown source. We have no evidence to indicate that this is the case, but an asymmetry small compared to that associated with field inhomogeneities might go unnoticed. Note that several common sources of line asymmetry are not present in our experiment: (a) No phase-sensitive detection is used in observing our signal. (b) The rf system is broadbanded, as evidenced by the fact that the oscillating field at 644 and 776 MHz differs by only about 3 dB; therefore, variation in proton-transition stimulation over the range of a line sweep (1 kHz maximum) is negligible. (c) Any linear variation over the course of an entire run, such as changing atomic flux, will be averaged out in forming symmetrized groups of sweeps for the subsequent analysis. Each point used in extrapolation is a symmetrized average of equal numbers of identical sweeps in opposite directions across the resonance line. In the absence of evidence to the contrary we neglect undetected asymmetry as an error source.

(*d*) *Other sources of systematic error.* Other sources of systematic error which have been considered include cavity pulling, the Bloch-Siegert effect and related pulling effects, second-order Doppler effect, and calibration error in the local frequency reference. All of these are small compared to the statistical error of the experiment.

(*e*) *Tests for consistency.* The two proton transition frequencies ν_{p1} and ν_{p2} are not independent. From Eq. (5) we have

$$\nu_{p1} + \nu_{p2} = \nu_0 \,. \tag{93}$$

Any error of the same sign in the proton frequencies will manifest itself by an erroneous value of the hyperfine frequency as determined from Eq. (93).

For purposes of comparison, the values of ν_{p1} and ν_{p2} obtained by the method of quadratic extrapolation were corrected to a common field (the ex-

TABLE III. Results for R. Errors are 1 standard deviation.

		fractional error
Results for quadratic extrapolation method		
R_1	658.210 7070 (44)	6.7×10^{-9}
R_2	658.210 7046 (19)	2.9×10^{-9}
Average	658.210 7063 (24)	3.3×10^{-9}
Results for linear extrapolation method		
R_1	658.210 7006 (104)	16×10^{-9}
R_2	658.210 7123 (49)	7×10^{-9}
Average	658.210 7065 (58)	9×10^{-9}
Final value		
$R = -g_j(\mathrm{H})/g_p(\mathrm{H}) = 658.210\,706(7)$		

TABLE IV. Determination of the hydrogen hyperfine frequency from $\nu_{p1}+\nu_{p2}$. (Values corrected to ν_e = 9201.000 MHz.)

ν_{p1}	=	644408376.38(10) Hz
ν_{p2}	=	775997375.46(04) Hz
ν_0	=	1420405751.84(11) Hz
Best experimental value (Ref. 19)		
ν_0	=	1420405751.768(2) Hz

perimental runs were carried out at slightly different fields). The results are given in Table IV. There is no apparent common error in ν_{p1} and ν_{p2}. The limit of error can be found by using the uncertainty in ν_0 from Table IV as a random error in the error propagation formula, Eq. (86). The conclusion is that any error which might shift ν_{p1} and ν_{p2} the same way can produce a fractional error in R of no more than 3.4×10^{-9}.

The question remains as to whether the values of R shown in Figs. 15 and 18 are truly distributed randomly. Since there is no significant discrepancy between R_1 and R_2, the results for all nineteen runs can be treated as coming from a distribution with a common mean. A normalized set of random variables was formed by taking the deviation of each result from the mean and dividing by the estimated statistical error for that individual measurement. A χ^2 test was then performed to compare the experimental data with what might be expected from a normal distribution. For the quadratic method of analysis the χ^2 test yields a probability of 30% that another equivalent set of data would deviate as much as that of Fig. 15. For the results reduced by the linear extrapolation method, Fig. 18, the probability is 95%. We interpret this to mean that with reasonable assurance the results can be treated as coming from a statistical distribution.

C. Final Results

Two sources of systematic error, spin exchange and wall shift, are known to cause opposite shifts in R_1 and R_2, and consequently the best value for the final result is a straight arithmetic average for the two transitions. The statistical error is $\delta R = \frac{1}{2}(\delta R_1^2+\delta R_2^2)^{1/2}$. Results are shown in Table III.

Since both extrapolation procedures yield the same value for R there is little to choose between them. However, their uncertainties differ considerably. The quadratic extrapolation method results in a standard deviation of 3.7×10^{-9}, while linear extrapolation yields a standard deviation of 9×10^{-9}. Because both results are based on the same data there is no justification for combining them in order to reduce the final standard deviation. On the other hand, there is no reason to increase the standard deviation of the best result simply because an alternative analysis procedure does not work so well. Consequently, the standard deviation of the final result, owing to statistical sources, is taken to be 3.7×10^{-9}.

The question remains as to our confidence in the results. When all is said and done, we have no real insight into the extrapolation procedure below the level of 1 part in 10^8. The numerical models are not convincing at that level, and the quality of the data is not good enough to resolve reasonable doubts about possible errors in extrapolation procedure. On this basis, we assign an estimated uncertainty of 1 part in 10^8. The final result is

$$R = -g_j(\mathrm{H})/g_p(\mathrm{H}) = 658.210\,706(6)\ . \tag{94}$$

The error is intended to represent a 68% confidence limit.

D. Correction to Free-Space Values

The effect of relativistic and radiative interactions on the g-factors of the electron and proton have been considered at length by Grotch and Hegstrom,[21] by Faustov,[22] and by Close and Osborne.[23] The results for hydrogenic atoms in the $1S$ state are

$$g_j(\mathrm{H}) = g_e\left[1-\frac{1}{3}(Z\alpha)^2\left(1-\frac{3}{2}\frac{m}{M}+\frac{3}{2}(1+Z)\frac{m^2}{M^2}\right)+\frac{1}{4\pi}\alpha(Z\alpha)^2\left(1-\frac{5}{3}\frac{m}{M}+\frac{6+Z}{3}\frac{m^2}{M^2}\right)\right]\ , \tag{95}$$

$$g_p(\mathrm{H}) = g_p\left(1-\frac{1}{3}(Z\alpha)^2+\frac{1}{6}Z\alpha^2\frac{m}{M}\frac{3+4a_p}{1+a_p}-\frac{1}{6}Z\alpha^2\frac{m^2}{M^2}\left(\frac{3(Z+1)+(6-Z)a_p}{1+a_p}\right)\right)\ , \tag{96}$$

where g_e and g_p are the g factor of the free electron and proton, respectively, and a_p is the anomalous proton moment in units of the nuclear magneton. If we retain terms $O(\alpha^2 m/M, \alpha^3)$, Eqs. (95) and (96) yield for hydrogen

$$\frac{g_e}{g_p} = \frac{g_j(\mathrm{H})}{g_p(\mathrm{H})}\left[1-\frac{1}{2}\alpha^2\frac{m}{M}\left(1-\frac{1}{3}\frac{3+4a_p}{1+a_p}\right)-\frac{\alpha^3}{4\pi}\right] = \frac{g_j(\mathrm{H})}{g_p(\mathrm{H})}(1-2.78\times10^{-8})\ . \tag{97}$$

Applying this result to Eq. (94) gives

$$g_e/g_p = -658.210\,688(7)\ . \tag{98}$$

Finally, we can correct for the anomalous moment of the electron to obtain the proton moment in Bohr magnetons. We use value of α^{-1} recommended by Taylor, Parker, and Langenberg in their

compilation of fundamental constants,[24] $\alpha^{-1} = 137.03602(21)$, and the following expression for the electron moment in Bohr magnetons:

$$\mu_e = -\mu_B[1 + \alpha/2\pi - 0.3285(\alpha/\pi)^2 + 0.13(\alpha/\pi)^3] = -\mu_B[1.001\,159\,639(3)] . \quad (99)$$

The uncertainty 0.3×10^{-9} includes contributions from α and the coefficient of α^3. Combining this with our value for $g_e/g_p = \mu_e/\mu_p$ yields the following result for the proton moment in Bohr magnetons:

$$\mu_p/\mu_B = 0.001\,521\,032\,181(15) . \quad (100)$$

E. Comparison with Previous Work

A summary of determinations of the proton moment in Bohr magnetons prior to 1969 is given by Langenberg, Parker, and Taylor.[25] We limit our discussion here to experiments which have some immediate connection to the present work.

Briefly, all previous experiments have utilized NMR to observe the proton moment. In order to obtain a value for the free proton, corrections must be made for the chemical shift, the diamagnetic effect of the host molecule, as well as for bulk diamagnetism of the sample. These corrections are large, typically 25 ppm, and not precisely known. Consequently, many of the previous experiments must now be interpreted in terms of the light they shed on the theory of chemical shifts.

One exception is the preliminary version of the present experiment.[26] The result

$$-g_j(\mathrm{H})/g_p(\mathrm{H}) = 658.210\,53(20) \quad (101)$$

agrees with our value, Eq. (94), to within the estimated error. The error, 30×10^{-8}, was set by the nonstatistical behavior of measurements made on different days, undoubtedly a result of the inhomogeneity shift which was identified subsequently

The most accurate related measurement is the determination of $g_j(\mathrm{H})g_p(\mathrm{H_2O})$ made by Lambe.[27] He compared an electron transition in hydrogen, as observed by microwave absorption of atomic hydrogen in a molecular-hydrogen buffer gas, with the NMR frequency of protons in a spherical water sample. His result is

$$-g_j(\mathrm{H})/g_p(\mathrm{H_2O}) = 658.215\,909(44) . \quad (102)$$

The apparent proton moment is related to the true moment by the chemical shielding constant σ as follows:

$$g_p(\text{apparent}) = g_p(1-\sigma) . \quad (103)$$

We can compare measurements of the proton in water and atomic hydrogen by the relation

$$\left[\frac{g_j(\mathrm{H})}{g_p(\mathrm{H})}\ \frac{g_j(\mathrm{H})}{g_p(\mathrm{H_2O})}\right]^{-1} = \frac{1-\sigma(\mathrm{H_2O})}{1-\sigma(\mathrm{H})} \cong 1-\sigma(\mathrm{H_2O})+\sigma(\mathrm{H}) . \quad (104)$$

The shielding constant for hydrogen (to order $\alpha^2 m/M$) is, from Eq. (96),

$$\sigma(\mathrm{H}) = \frac{1}{3}\alpha^2\left(1-\frac{1}{2}\frac{m}{M}\frac{3+4a_p}{1+a_p}\right) = 17.733\times 10^{-6} . \quad (105)$$

By combining Eqs. (94), (102), and (105), we obtain

$$\sigma(\mathrm{H_2O}) = 25.64(7)\times 10^{-6} . \quad (106)$$

Although the shielding constant for water cannot be compared directly with theory, it provides a useful link to $\sigma(\mathrm{H_2})$, for which an accurate theoretical value exists. Comparisons of the NMR frequency of the proton in molecular hydrogen and water[28] yields $\sigma(\mathrm{H_2O}) - \sigma(\mathrm{H_2}) = -0.6(3)\times 10^{-6}$, from which it follows that

$$\sigma(\mathrm{H_2}) = 26.2(3)\times 10^{-6} . \quad (107)$$

The general theory for magnetic shielding in polyatomic molecules was first developed by Ramsey[29] who showed that the shielding constant can be written as the sum of two terms:

$$\sigma = \sigma^{\mathrm{dia}} + \sigma^{\mathrm{para}} , \quad (108)$$

where σ^{dia} represents the simple diamagnetic shielding effect of the electrons in the molecule and σ^{para} arises from second order paramagnetic effects. Newell[30] has obtained

$$\sigma^{\mathrm{dia}}(\mathrm{H_2}) = 32.1(1)\times 10^{-6} . \quad (109)$$

The best value for the paramagnetic term is from the work of Ramsey and his co-workers[31]:

$$\sigma^{\mathrm{para}}(\mathrm{H_2}) = -5.9(3)\times 10^{-6} . \quad (110)$$

Combining the results gives

$$\sigma(\mathrm{H_2}) = 26.2(3)\times 10^{-6} , \quad (111)$$

in exact agreement with the measured value, Eq. (107). However, the experimental resolution is only 0.3 ppm. It could readily be increased by a new comparison of the proton in molecular hydrogen and in water (or, preferably, a more reliable NMR standard) and it appears possible to improve the theoretical value of $\sigma(\mathrm{H_2})$ by obtaining more precise data on the spin-rotation interaction in hydrogen.[32] Thus it appears that the topic of chemical shifts in simple molecules is ripe for a more detailed elaboration.

In Lambe's experiment, as well as in earlier work, the chief difficulty lay in observing the electron resonance in atomic hydrogen. Klein[33] sidestepped this problem by determining the cyclotron frequency of electrons in a field which is calibrated by NMR. The result is

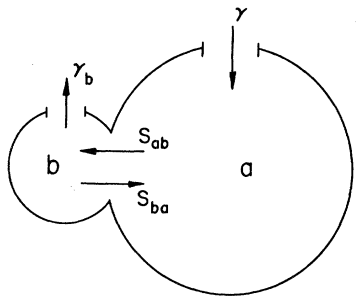

FIG. 19. Flow parameters for the two-region model.

$$\omega_e/\omega_p(H_2O) = 657.465\,07(32) \ .$$

We can express this in terms of μ_B/μ_p by utilizing Eqs. (103) and (106) to obtain

$$\frac{\mu_p}{\mu_B}(\text{Klein}) = 0.001\,521\,0328(8) \ . \tag{112}$$

A comparison of Klein's value for μ_p/μ_B with our value, Eq. (100), can serve as a check on our understanding of the anomalous moment of the electron. Unfortunately, although the two values overlap, the uncertainty in Klein's result is too large to improve our knowledge of the electron moment anomaly.

ACKNOWLEDGMENTS

We wish to acknowledge the contributions of Hugh G. Robinson in the early stages of this work, both in the design of the experiment and in construction of the apparatus. We are indebted to Norman F. Ramsey for several valuable discussions.

APPENDIX A: GOVERNING EQUATIONS FOR INHOMOGENEITY FREQUENCY SHIFT

Following Brenner[13] we subdivide the system into two volumes between which atoms flow as described by simple rate processes. Fig. (19) illustrates the model and the flow parameters. Volume a (the storage bulb) is assumed to be large compared to volume b (the stem). N_a and N_b represent the instantaneous number of atoms in volumes a and b, respectively. The atomic flux from a to b is $N_a S_{ab}$, and the flux from b to a is $N_b S_{ba}$. The incident flux rate is $\gamma(N_a + N_b)$. If we let $w = N_b/N_a$, then it follows that at equilibrium

$$w = S_{ab}/(S_{ba} + \gamma_b) \ , \tag{A1}$$

$$\gamma_b/\gamma = 1 + 1/w \ . \tag{A2}$$

The inhomogeneity shift of interest here occurs when both the static magnetic field and the amplitude of the rf (proton) field have different values in the two regions.

The departures of the oscillating fields from resonance are given by

$$\delta_a = \omega - \omega_{0a} \ , \quad \Delta_a = \Omega - \Omega_{0a} \ ,$$

where ω_{0a}, Ω_{0a} are, respectively, the resonance frequency of the electron and proton in region a. Similar notation applies to region b.

The rf-field amplitude in the two regions is denoted by X_b, X_a. We write density-matrix rate equations as in Sec. II B, except that the field relaxation terms, Eq. (13), are omitted since this effect should follow from our model. The matrix elements in the two regions are treated independently and are denoted by a superscript a or b. The rate equations analogous to Eq. (25) are

$$\begin{aligned}
&\dot{\mathcal{P}}_1^a = -S_{ab}\mathcal{P}_1^a + wS_{ba}\mathcal{P}_1^b - 2X_a D_2^a + 2K(\alpha D_4^a - \beta D_3^a) \ , \\
&\dot{\mathcal{P}}_2^a = -S_{ab}\mathcal{P}_2^a + wS_{ba}\mathcal{P}_2^b + X_a D_2^a - 4K(\alpha D_4^a - \beta D_3^a) + \tfrac{1}{2}\gamma(1+w) \ , \\
&\dot{D}_1^a = -S_{ab} D_1^a + wS_{ba} D_1^b - \Delta_a D_2^a + K(\beta D_5^a - \alpha D_6^a) \ , \\
&\dot{D}_2^a = -S_{ab} D_2^a + wS_{ba} D_2^b + \Delta_a D_1^a + \tfrac{1}{2}X_a \mathcal{P}_1^a + K(\alpha D_5^a + \beta D_6^a) \ , \\
&\dot{D}_3^a = -S_{ab} D_3^a + wS_{ba} D_3^b - \delta_a D_4^a + \tfrac{1}{2}X_a D_6^a - K\beta\mathcal{P}_2^a \ , \\
&\dot{D}_4^a = -S_{ab} D_4^a + wS_{ba} D_4^b + \delta_a D_3^a - \tfrac{1}{2}X_a D_5^a + K\alpha\mathcal{P}_2^a \ , \\
&\dot{D}_5^a = -S_{ab} D_5^a + wS_{ba} D_5^b - (\Delta_a + \delta_a) D_6^a + \tfrac{1}{2}X_a D_4^a - K(\beta D_1^a + \alpha D_2^a) \ , \\
&\dot{D}_6^a = -S_{ab} D_6^a + wS_{ba} D_6^b + (\Delta_a + \delta_a) D_5^a - \tfrac{1}{2}X_a D_3^a + K(\alpha D_1^a - \beta D_2^a) \ , \\
&\dot{\mathcal{P}}_1^b = -[S_{ba} + \gamma_b)\mathcal{P}_1^b + (1/w) S_{ab}\mathcal{P}_1^a - 2X_b D_2^b + 2K(\alpha D_4^b - \beta D_3^b] \ , \\
&\dot{\mathcal{P}}_2^b = -(S_{ba} + \gamma_b)\mathcal{P}_2^b + (1/w) S_{ab}\mathcal{P}_2^a + X_b D_2^b - 4K(\alpha D_4^b - \beta D_3^b) \ ; \\
&\dot{D}_1^b = -(S_{ba} + \gamma_b) D_1^b + (1/w) S_{ab} D_1^a - \Delta_b D_2^b + K(\beta D_5^b - \alpha D_6^b) \ ,
\end{aligned} \tag{A3}$$

TABLE V. Representation transformation matrix $\Gamma = \langle S, M_S; m_{I1}, m_{I2} | m_{S1}, m_{I1}; m_{S2}, m_{I2} \rangle$. $+ \Rightarrow +\frac{1}{2}$; $- \Rightarrow -\frac{1}{2}$.

$S, M_S; m_{I1}, m_{I2}$ \ $m_{S1}m_{I1}$ / $m_{S2}m_{I2}$	++ ++	++ +−	++ −−	++ −+	+− +−	+− ++	+− −−	+− −+	−− ++	−− +−	−− −−	−− −+	−+ ++	−+ +−	−+ −−	−+ −+
1, 1; ++	1															
1, 1; +−		1														
1, 1; −−					1											
1, 1; −+						1										
1, 0; ++			$1/\sqrt{2}$										$1/\sqrt{2}$			
1, 0; +−		$1/\sqrt{2}$												$1/\sqrt{2}$		
1, 0; −−					$1/\sqrt{2}$					$1/\sqrt{2}$						
1, 0; −+						$1/\sqrt{2}$			$1/\sqrt{2}$							
1, −1; ++																1
1, −1; +−															1	
1, −1; −−											1					
1, −1; −+												1				
0, 0; ++			$1/\sqrt{2}$										$-1/\sqrt{2}$			
0, 0; +−		$1/\sqrt{2}$												$-1/\sqrt{2}$		
0, 0; −−					$1/\sqrt{2}$					$-1/\sqrt{2}$						
0, 0; −+						$1/\sqrt{2}$			$-1/\sqrt{2}$							

$$
\begin{aligned}
\dot{D}_2^b &= -(S_{ba}+\gamma_b) D_2^b + (1/w) S_{ab} D_2^a + \Delta_b D_1^b + \tfrac{1}{2} X_b \mathcal{P}_1^b + K(\alpha D_5^b + \beta D_6^b) , \\
\dot{D}_3^b &= -(S_{ba}+\gamma_b) D_3^b + (1/w) S_{ab} D_3^a - \delta_b D_4^b + \tfrac{1}{2} X_b D_6^b - K\beta \mathcal{P}_2^b) \\
\dot{D}_4^b &= -(S_{ba}+\gamma_b) D_4^b + (1/w) S_{ab} D_4^a + \delta_b D_3^b - \tfrac{1}{2} X_b D_5^b + K\alpha \mathcal{P}_2^b , \\
\dot{D}_5^b &= -(S_{ba}+\gamma_b) D_5^b + (1/w) S_{ab} D_5^a - (\Delta_b + \delta_b) D_6^b + \tfrac{1}{2} X_b D_4^b - K(\beta D_1^b + \alpha D_2^b) , \\
\dot{D}_6^b &= -(S_{ba}+\gamma_b) D_6^b + (1/w) S_{ab} D_6^a + (\Delta_b + \delta_b) D_5^b - \tfrac{1}{2} X_b D_3^b + K(\alpha D_1^b - \beta D_2^b) .
\end{aligned}
\tag{A4}
$$

The dimensionless microwave field is given by

$$
\begin{aligned}
\alpha &= [1/(1+w)] (D_4^a + w D_4^b) , \\
\beta &= [1/(1+w)] (D_3^a + w D_3^b) ,
\end{aligned}
\tag{A5}
$$

analogous to Eqs. (20) and (24), and is assumed to be the same in both regions. (Relaxation of this restriction has been found to have no appreciable effect.) Cavity mistuning has been shown to have essentially the same effect for two regions as for the single-region model, and so we neglect it here. The results of a computer analysis of these equations is given in Sec. II E, where we have taken

$$
\tau = S_{ab}^{-1} , \quad \delta_0 = \omega_{0a} - \omega_{0b} .
$$

APPENDIX B: SPIN-EXCHANGE CONTRIBUTIONS TO RATE EQUATIONS

We wish to obtain the contribution of spin exchange to the rate equations for the density matrix. The treatment outlined here follows the arguments of Bender.[7] The method of Balling, Hanson, and Pipkin[14] gives virtually identical results.

We are interested in the effect of a collision of two atoms. Initially each of the atoms is described by a 4×4 density matrix ρ^i in the (m_S, m_I) representation. The 16×16 density matrix for the pair of atoms in the $(m_{S1}, m_{I1}; m_{S2}, m_{I2})$ representation is the direct product of ρ^i with itself:

$$
\sigma^i = \rho^i \otimes \rho^i . \tag{B1}
$$

During the collision the electron spins are strongly coupled so that they are naturally represented by (S, M_S) rather than by (m_{S1}, m_{S2}). We assume that the interaction between nuclei is small, and that m_{I1} and m_{I2} remain good quantum numbers. Transformations of σ^i from the $(m_{S1}, m_{I1}; m_{S2}, m_{I2})$ to the $(S, M_S; m_{I1}, m_{I2})$ representation is accomplished by the unitary transformation Γ given in Table V:

$$
\sigma^{ci} = \Gamma \sigma^i \Gamma^* . \tag{B2}
$$

The collision process is described by a second unitary transformation A, to give a post-collision density matrix σ^{cf}:

TABLE VI. Matrix $C = \Gamma^* B \Gamma$. (j_1, j_2) identify $(m_{S1}, m_{I1}; m_{S2}, m_{I2})$, where j refers to the states of Fig. 1.

j_1, j_2	1,1	1,2	1,3	1,4	2,1	2,2	2,3	2,4	3,1	3,2	3,3	3,4	4,1	4,2	4,3	4,4
1,1																
1,2																
1,3		1												−1		
1,4			1										−1			
2,1																
2,2																
2,3					1			−1								
2,4						1	−1									
3,1						−1		1								
3,2					−1		1									
3,3																
3,4																
4,1			−1											1		
4,2		−1													1	
4,3																
4,4																

$$\sigma^{cf} = A \sigma^{ci} A^* \,. \tag{B3}$$

A is simply a diagonal matrix, with $S=1$ (triplet) elements $e^{-i\Delta_3}$, and $S=0$ (singlet) elements $e^{-i\Delta_1}$. Since A is unitary we can without loss of generality factor out $e^{-i\Delta_3}$ and write

$$A = I - \tfrac{1}{2} x B \,,$$

where

$$x = 1 - e^{i\Delta} = 1 - e^{-i(\Delta_1 - \Delta_3)} \,. \tag{B4}$$

I is the identity matrix; B is a matrix all of whose elements are zero except the last four diagonal elements, which are 2.

Finally, we transform back to the original $(m_{S1}, m_{I1}; m_{S2}, m_{I2})$ representation. We have

$$\begin{aligned}
\sigma^f &= \Gamma^* \sigma^{cf} \Gamma \\
&= \Gamma^* A \Gamma \sigma^i \Gamma^* A^* \Gamma \\
&= \Gamma^* (I - \tfrac{1}{2} x B) \Gamma \sigma^i \Gamma^* (I - \tfrac{1}{2} x^* B^*) \Gamma \\
&= (I - \tfrac{1}{2} x C) \sigma^i (I - \tfrac{1}{2} x^* C^*) \\
&= \sigma^i - \tfrac{1}{2}(x C \sigma^i + x^* \sigma^i C^*) + \tfrac{1}{4} |x|^2 C \sigma^i C^* \,,
\end{aligned} \tag{B5}$$

where $C = \Gamma^* B \Gamma$. C is displayed in Table VI. Since $C^* = C$, and $|x|^2 = 2(1 - \cos\Delta)$, we have

$$\sigma^f = \sigma^i - \tfrac{1}{2}(1 - \cos\Delta)\, C \sigma^i + \sigma^i C - C \sigma^i C - \tfrac{1}{2} i \sin\Delta (\sigma^i C - C \sigma^i) \,. \tag{B6}$$

In order to recover a 4×4 density matrix we ignore the correlation between the two atoms which have just collided and trace over atom number 1:

$$\rho^{ft}(j_2, j_2') \sum_{j_1, j_1'} \delta(j_1, j_1')\, \sigma^f(j_1 j_2, j_1' j_2') \,. \tag{B7}$$

We must average over the time at which the collisions occur. If an element of ρ^{ft} contains a term of frequency large compared to the reciprocal of the mean time between collisions, then the contribution of that term to the final density matrix ρ^f will be zero. This eliminates all terms which have a frequency different from the element under consideration.

Carrying out the above prescription for our density matrix ρ, we obtain the values for ρ^f given in Table VII. Here we revert to labeling the elements by the level numbers of Fig. 1. The result represents the change in the density matrix due to a single collision in terms of the phase angle Δ. In order to obtain the average rate of change of ρ due to spin exchange, we integrate over possible impact parameters R. The results are most conveniently expressed in terms of the collision rates U and V:

$$\begin{aligned}
U &= \tfrac{1}{2} n \langle v_{\rm rel} \rangle \int_0^\infty [1 - \cos\Delta(R)]\, 2\pi R\, dR \,, \\
V &= \tfrac{1}{2} n \langle v_{\rm rel} \rangle \int_0^\infty \sin\Delta(R)\, 2\pi R\, dR \,.
\end{aligned} \tag{B8}$$

The spin-exchange contributions to the rate equations

$$\begin{aligned}
\dot\rho_{11} &= -U(\rho_{11}\rho_{33} - \rho_{22}\rho_{44}) \,, \\
\dot\rho_{22} &= U(\rho_{11}\rho_{33} - \rho_{22}\rho_{44}) \,, \\
\dot\rho_{33} &= -U(\rho_{11}\rho_{33} - \rho_{22}\rho_{44}) \,, \\
\dot\rho_{44} &= U(\rho_{11}\rho_{33} - \rho_{22}\rho_{44}) \,,
\end{aligned}$$

TABLE VII. Density-matrix elements after collision with another hydrogen atom having the same initial density matrix.

$$\rho_{11}^f = \rho_{11} - \tfrac{1}{2}(1-\cos\Delta)(\rho_{11}\rho_{33} - \rho_{22}\rho_{44})$$

$$\rho_{22}^f = \rho_{22} + \tfrac{1}{2}(1-\cos\Delta)(\rho_{11}\rho_{33} - \rho_{22}\rho_{44})$$

$$\rho_{33}^f = \rho_{33} - \tfrac{1}{2}(1-\cos\Delta)(\rho_{11}\rho_{33} - \rho_{22}\rho_{44})$$

$$\rho_{44}^f = \rho_{44} + \tfrac{1}{2}(1-\cos\Delta)(\rho_{11}\rho_{33} - \rho_{22}\rho_{44})$$

$$\rho_{12}^f = \rho_{12} - \tfrac{1}{2}(1-\cos\Delta)(\rho_{33}+\rho_{44})\rho_{12} + \tfrac{1}{2}i(\sin\Delta)(\rho_{13}\rho_{23}^* - \rho_{14}\rho_{24}^*)$$

$$\rho_{13}^f = \rho_{13} - \tfrac{1}{2}(1-\cos\Delta)(\rho_{13} - \rho_{12}\rho_{23} - \rho_{14}\rho_{34}^*) + \tfrac{1}{2}i(\sin\Delta)\{[1-2(\rho_{11}+\rho_{22})]\rho_{13} + \rho_{12}\rho_{23} - \rho_{14}\rho_{34}^*\}$$

$$\rho_{14}^f = \rho_{14} - \tfrac{1}{2}(1-\cos\Delta)(\rho_{22}+\rho_{33})\rho_{14} + \tfrac{1}{2}i(\sin\Delta)(\rho_{33}-\rho_{22})\rho_{14}$$

$$\rho_{23}^f = \rho_{23} - \tfrac{1}{2}(1-\cos\Delta)(\rho_{11}+\rho_{44})\rho_{23} + \tfrac{1}{2}i(\sin\Delta)(\rho_{44}-\rho_{11})\rho_{23}$$

$$\rho_{24}^f = \rho_{24} - \tfrac{1}{2}(1-\cos\Delta)(\rho_{24} - \rho_{12}^*\rho_{14} - \rho_{23}\rho_{34}) + \tfrac{1}{2}i(\sin\Delta)\{[1-2(\rho_{11}+\rho_{22})]\rho_{24} + \rho_{12}^*\rho_{14} - \rho_{23}\rho_{34}\}$$

$$\rho_{34}^f = \rho_{34} - \tfrac{1}{2}(1-\cos\Delta)(\rho_{11}+\rho_{22})\rho_{34} + \tfrac{1}{2}i(\sin\Delta)(\rho_{13}^*\rho_{14} - \rho_{23}^*\rho_{24})$$

$$\dot{\rho}_{12} = -U(\rho_{33}+\rho_{44})\rho_{12} + iV(\rho_{13}\rho_{23}^* - \rho_{14}\rho_{24}^*) ,$$

$$\dot{\rho}_{13} = -U(\rho_{13} - \rho_{12}\rho_{23} - \rho_{14}\rho_{34}^*) + iV\{[1-2(\rho_{11}+\rho_{22})]\rho_{13} + \rho_{12}\rho_{23} - \rho_{14}\rho_{34}^*\}$$

$$\dot{\rho}_{14} = -U(\rho_{22}+\rho_{33})\rho_{14} + iV(\rho_{33}-\rho_{22})\rho_{14} ,$$

$$\dot{\rho}_{23} = -U(\rho_{11}+\rho_{44})\rho_{23} + iV(\rho_{44}-\rho_{11})\rho_{23} ,$$

$$\dot{\rho}_{24} = -U(\rho_{24} - \rho_{12}^*\rho_{14} - \rho_{23}\rho_{34}) + iV\{[1-2(\rho_{11}+\rho_{22})]\rho_{24} + \rho_{12}^*\rho_{14} - \rho_{23}\rho_{34}\} ,$$

$$\dot{\rho}_{34} = -U(\rho_{11}+\rho_{22})\rho_{34} + iV(\rho_{13}^*\rho_{14} - \rho_{23}^*\rho_{24}) . \qquad \text{(B9)}$$

Alternatively, a completely quantum-mechanical treatment[14] gives the same result with the identifications

$$U = n\langle v_{\rm rel}\rangle\sigma_{\rm ex} ,$$
$$V = n\langle v_{\rm rel}\rangle\sigma_{\rm ex} , \qquad \text{(B10)}$$

where $\sigma_{\rm ex}$ is the exchange cross section

$$\sigma_{\rm ex} = \langle v_{\rm rel}\rangle^{-1}\frac{\pi\hbar}{\mu k}\sum_{e=0}^{\infty}(2l+1)\sin^2(\delta_e^3 - \delta_e^1) \qquad \text{(B11)}$$

and κ is the frequency shift parameter given by

$$\kappa\sigma_{\rm ex} = \langle v_{\rm rel}\rangle^{-1}\frac{\pi\hbar}{\mu k}\sum_{e=0}^{\infty}[1+(-1)^e][2l+1]\sin^2(\delta_e^3 - \delta_e^1) . \qquad \text{(B12)}$$

δ_e^3 and δ_e^1 are, respectively, the singlet and triplet phase shifts; μ is the reduced mass. The brackets indicate an average of over momentum, $\hbar k$.

Our computations used the measured value[34] of $\sigma_{\rm ex}$, $28.5(43)\times10^{-16}$ cm^2, which is in reasonable agreement with theoretical estimates.[35] For κ we used Bender's estimate,[14] $\kappa = 0.2$.

*Work supported by the Joint Services Electronics Program under Contract No. DA28-043-AMC-02536(E), the Office of Naval Research, and the MIT Sloan Fund.

†National Science Foundation Predoctoral Fellow, Harvard University, Cambridge, Mass. Present address: Middlebury College, Middlebury, Vt.

‡Also, Department of Physics, Massachusetts Institute of Technology, Cambridge, Mass.

§Present address: Department of Physics, Williams College, Williamstown, Mass.

[1]T. Myint, D. Kleppner, N. F. Ramsey, H. G. Robinson, Phys. Rev. Letters 17, 405 (1966).

[2]P. F. Winkler, F. G. Walther, M. T. Myint, and D. Kleppner, *Physics of One- and Two-Electron Atoms*, edited by F. Bopp and H. Kleinpoppen (North-Holland, Amsterdam, 1969), p. 146.

[3]D. Kleppner, in *Proceedings of the First International Conference on Precision Measurements and Fundamental Constants, Gaithersberg, Maryland*, 1970 (Natl. Bur. Std., Washington, D. C., to be published).

[4]T. Myint, Ph. D. thesis (Harvard University, 1966) (unpublished).

[5]P. F. Winkler, Ph. D. thesis (Harvard University, 1970) (unpublished).

[6]N. F. Ramsey, *Molecular Beams* (Oxford U. P., London, 1956), p. 84.

[7]P. L. Bender, Phys. Rev. 132, 2154 (1963).

[8]S. B. Crampton, H. G. Robinson, D. Kleppner, N. F. Ramsey, Phys. Rev. 141, 55 (1966).

[9]C. P. Slichter, *Principles of Magnetic Resonance* (Harper and Row, New York, 1963), Chap. 5.

[10]D. Kleppner, H. M. Goldenberg, and N. F. Ramsey, Phys. Rev. 126, 603 (1962).

[11]N. Bloembergen, E. M. Purcell, R. V. Pound, Phys. Rev. 73, 679 (1948).

[12]F. G. Walther, W. D. Phillips, and D. Kleppner (unpublished).

[13]D. Brenner, Phys. Rev. 185, 26 (1969).

[14]L. C. Balling, R. J. Hanson, and F. M. Pipkin, Phys. Rev. 133, A607 (1964); S. B. Crampton, *ibid.* 158, 57 (1967).

[15]S. B. Crampton, J. A. Duvivier, G. S. Read, and E. R. Williams, Bull. Am. Phys. Soc. 16, 85 (1971); H. C. Berg, Phys. Rev. 137, A1621 (1965); C. Audoin, Phys. Letters 28A, 372 (1968); H. Hellwig, Phys. Rev. 166, 4 (1968).

[16]N. F. Ramsey, Phys. Rev. 100, 1191 (1955).

[17]D. Kleppner, H. C. Berg, S. B. Crampton, N. F. Ramsey, R.F.C. Vessot, H. E. Peters, and J. Vanier, Phys. Rev. 138, A972 (1965).

[18]We are indebted to Hugh G. Robinson for the design and construction of these shims.

[19]H. Hellwig, R. F. C. Vessot, M. W. Lecine, P. W. Zitzewitz, D. W. Allen, J. W. Glaze, IEEE Trans. Instr. Meas. 1M-19, 200 (1970).

[20]P. Zitzewitz, E. Uzgiris, and N. F. Ramsey, Rev. Sci. Instr. 41, 81 (1970).

[21]H. Grotch and R. A. Hegstrom, Phys. Rev. A 4, 59 (1971).

[22]R. Faustov, Phys. Letters 33B, 422 (1970).

[23]F. E. Close and H. Osborne, Phys. Letters 34B, 400 (1971).
[24]B. N. Taylor, W. H. Parker, and D. N. Langenberg, Rev. Mod. Phys. 41, 375 (1969).
[25]Ref. 24, Table VII.
[26]Ref. 1. The value given here is increased 6×10^{-8} from the reported value because of a subsequently discovered error in converting the time standard from the UT2 to A1 time scales.
[27]E. B. D. Lambe, *Polarization, Matiere et Rayonnement* (Societe Francaise de Physique, Paris, 1969), p. 441.
[28]H. A. Thomas, Phys. Rev. 80, 901 (1950); W. A. Hardy, private communication quoted in S. Liebes, Jr. and P. A. Franken, Phys. Rev. 116, 633 (1959).
[29]N. F. Ramsey, Phys. Rev. 78, 699 (1950).
[30]G. F. Newell, Phys. Rev. 80, 476 (1950).
[31]N. J. Harrick, R. G. Barnes, P. J. Bray, and N. F. Ramsey, Phys. Rev. 90, 260 (1953).
[32]N. F. Ramsey (private communication).
[33]E. Klein, Z. Physik 208, 28 (1968).
[34]A. F. Hildebrandt, F. B. Booth, and C. A. Barth, J. Chem. Phys. 31, 273 (1959); R. M. Mazo, *ibid.* 34, 169 (1961).
[35]A. Dalgarno, Proc. Roy. Soc. (London) A262, 132 (1961); F. J. Smith, Planetary Space Sci. 11, 1126 (1963).

PHYSICAL REVIEW A VOLUME 5, NUMBER 1 JANUARY 1972

Radial Momentum Distributions $I_0(p)$ and Compton Profiles $J(q)$. The ^1S Be Atom Ground State*†

Robert Benesch
Department of Applied Analysis and Computer Science, University of Waterloo, Waterloo, Ontario, Canada

and

Vedene H. Smith, Jr.
Department of Chemistry, Queen's University, Kingston, Ontario, Canada
(Received 4 May 1971)

The natural orbitals (NO) obtained from ^1S Be atom ground-state wave functions which incorporate various amounts of the correlation energy are Fourier transformed to momentum space in order to obtain radial momentum distributions $I_0(p)$. Momentum distributions calculated from several analytical restricted Hartree-Fock (RHF) wave functions are also presented. Correlated and RHF Compton profile values $J(q)$ are found to be in better agreement than the corresponding $I_0(p)$ values. In the "valence shell" portion of the $I_0(p)$ distribution, relative differences as large as 25% are observed between correlated and RHF values, whereas in the "core" portion of $I_0(p)$ the correlated and RHF values are in relatively good agreement. The virial theorem is used to explain the differences observed between correlated and RHF $I_0(p)$ distributions. Basis set effects are found to be negligible in comparison with correlation effects. The present calculations indicate that much of the discrepancy between correlated and RHF $I_0(p)$ values, at least for the ^1S Be ground state, is due to the $2s$-$2p$ "near-degeneracy" effect. They also demonstrate that the node found when examining the long-range behavior of the RHF $1s$ orbital in position space is of a spurious nature.

I. INTRODUCTION

In order to assess the importance of electron correlation effects on free-atom radial momentum distributions $I_0(p)$ and Compton profiles $J(q)$, a series of calculations has been initiated for those atomic systems for which "accurate" correlated wave functions are available. The first papers[1] of this study (collectively referred to as I) demonstrated that correlated $I_0(p)$'s can be very easily obtained by Fourier transforming to momentum space the natural spin orbitals (NSO) or the natural orbitals (NO) obtained from the 1-matrix analysis or from the charge-density matrix analysis, respectively, of given position-space wave functions.

The density-matrix formalism developed in I was applied there to the He atom[1(a)] and to the Li^+ ion[1(b)] in their ^1S ground states. It was observed that the correlated and restricted Hartree-Fock (RHF) $I_0(p)$'s were in good agreement. In Paper II,[2] $I_0(p)$'s were determined for the ^2S ground state of the Li atom from several independent particle-model (IPM) wave functions and from the NO analysis of a highly accurate Hylleraas-type wave function. For Li it was observed that in the "valence shell" portion of the $I_0(p)$ distribution, relative differences of the order 2–3% exist between correlated and RHF values whereas good agreement was found between IPM and correlated results for the inner shell or "core" portion of